

Computational Study of Fluidic Thrust Vectoring Using Shock Vector and Separation Control

A project present to
The Faculty of the Department of Aerospace Engineering
San Jose State University

in partial fulfillment of the requirements for the degree
Master of Science in Aerospace Engineering

By

Amir Yahaghi

May 2011

approved by

Dr. Periklis Papadopoulos
Faculty Advisor



San José State
UNIVERSITY

©2011
Amir Yahaghi
ALL RIGHTS RESERVED

Abstract

A computational investigation of a recessed cavity nozzle was completed to evaluate the use of fluidic throat shifting and external shock vector within the same nozzle. Steady state computations for axisymmetric and 2-Dimensional nozzles with and without secondary injections were completed to confirm the ability of ANSYS Fluent calculating the flow through a dual throat nozzle for unsteady state conditions. This nozzle was designed using a recessed cavity to improve throat shifting method. A Tertiary injection at the second throat was added to act as a shock vector control at exit conditions. The 2D nozzle selected for this study has been proven for the best experimental configuration tested to date by NASA Langley¹. The nozzle design variables include several fluidic injection angles of tertiary injection at the exit line and post exit conditions. All simulations were conducted using a freestream Mach of 0.1 at different nozzle pressure ratios.

Internal nozzle performance and thrust vectoring angles were calculated for 6 different configurations over the range of nozzle pressure ratios from 3 – 8. All secondary and tertiary injections included a 2.8% mass flow rate of the primary nozzle. The computational results indicate that increasing the tertiary injection angle for external and exit line injections will increase the thrust vectoring angles with a decrease in the internal nozzle performance. It was also concluded that the tertiary exit line injections further skew the sonic line at the second throat instead of creating a shock. Therefore, decreasing the internal nozzle performance much less than predicted.

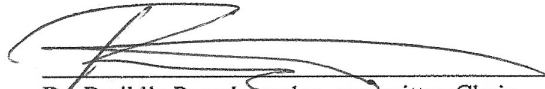
San Jose State University

The Undersigned Committee Approves

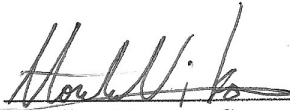
**COMPUTATIONAL STUDY OF FLUIDIC THRUST VECTORING
USING SHOCK VECTOR AND SEPARATION CONTROL**

By
Amir Yahaghi

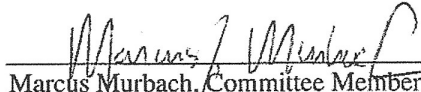
APPROVED FOR THE DEPARTMENT OF MECHANICAL AND AEROSPACE ENGINEERING



Dr. Periklis Papadopoulos, committee Chair
San Jose State University



Dr. Nikos Mourtos, Committee Member
San Jose State University



Marcus Murbach, Committee Member
NASA Ames Research center

Acknowledgements

I would like to take the opportunity to thank those who provided me their guidance through my educational career at San Jose State University. I would like to specifically thank Dr. Periklis Papadopoulos, Dr. Nikos Mourtos, and Marcus Murbach for their support through my graduate and undergraduate studies. Finally, I like to thank all friends and family for their support and encouragement through my education career.

Table of Contents

<u>Abstract.....</u>	<u>iii</u>
<u>Acknowledgements.....</u>	<u>v</u>
<u>List of Figures.....</u>	<u>1</u>
<u>List of Tables.....</u>	<u>4</u>
<u>Nomenclature.....</u>	<u>5</u>
<u>I. Introduction.....</u>	<u>8</u>
<u>II. Experimental Method.....</u>	<u>12</u>
<u>A. Axisymmetric Model.....</u>	<u>13</u>
<u>B. 2 Dimensional Results.....</u>	<u>13</u>
<u>II. Computational Method.....</u>	<u>15</u>
<u>A. Governing equations.....</u>	<u>15</u>
<u>B. Solver Setting, ANSYS Fluent.....</u>	<u>17</u>
<u>C. Performance calculation.....</u>	<u>18</u>
<u>D. Nozzle Geometry.....</u>	<u>21</u>
<u>E. Grid Generation.....</u>	<u>24</u>
<u>F. Boundary conditions.....</u>	<u>28</u>
<u>1. Axisymmetric Geometry.....</u>	<u>28</u>
<u>2. 2 Dimensional Geometry.....</u>	<u>28</u>
<u>III. Results.....</u>	<u>30</u>

A. <u>Axisymmetric Nozzle</u>	30
B. <u>Preliminary 2D Nozzle</u>	37
C. <u>2D Nozzle</u>	39
1. <u>Experimental and Computational Comparison</u>	40
2. <u>Effects of external tertiary injection</u>	49
3. <u>Effects of tertiary injection at exit line</u>	57
4. <u>Comparison of the external and exit line injection</u>	65
<u>Conclusion</u>	67
<u>References</u>	68
<u>Appendix</u>	Error! Bookmark not defined.

List of Figures

Figure 1: Pratt and Whitney F-199-PW-100 ¹⁰	8
Figure 2: Eurojet EJ200 ¹⁵	8
Figure 3: Shock Vector Control ²	9
Figure 4: Throat Shifting Method ¹⁰	9
Figure 5: Counterflow Thrust Vectoring ³	10
Figure 6: Dual Throat Nozzle with fluidic injection at upstream throat ⁵	10
Figure 7: NASA Langley Research Center 2D DTN Fluidic thrust nozzle installed in the Jet Exit Test Facility ¹⁷	12
Figure 8: NSASA Langley Research Center axisymmetric DTN installed in the Jet Exit Test Facility ⁵	12
Figure 9: Geometry for DTN nozzle with no injections. Figure not to scale.....	13
Figure 10: Geometry of DTN nozzle with injections. Figure not to scale.....	23
Figure 11: Some views of computational mesh generated using GridPro.....	26
Figure 12: Boundary condition for axisymmetric nozzles. Configuration 1-3.....	29
Figure 13: Boundary conditions for 2D nozzles. Configurations 4-13.....	29
Figure 14: Comparison of experimental and computational results, system thrust ratio.....	31
Figure 15: Comparison of experimental and computational results, discharge ratio.....	31
Figure 16: Computational Mach Contour, NPR 1.89, no injection.....	32
Figure 17: Computational Mach Contour, NPR 6, no injection.....	32

Figure 18: Computational Mach Contour, NPR 10, no injection.....32

Figure 19: Total Pressure Contours, NPR 1.89, no injection.....35

Figure 20: Total Pressure Contours, NPR 6, no injection.....35

Figure 21: Total Pressure Contours, NPR 10, no injection.....	35
Figure 22: Total Temperature Contours, NPR 1.89, no injection.....	36
Figure 23: Total Temperature Contours, NPR 6, no injection.....	36
Figure 24: Total Temperature Contours, NPR 10, no injection.....	36
Figure 25: Velocity Magnitudes at exit, showing the capturing of boundary layer.....	37
Figure 26: Mach contours for configurations 4 and 5.....	37
Figure 27: Comparison of experimental and computational nozzle performance, configuration 6.	
No injection.....	41
Figure 28: Mach contours for Configuration 6, no injection.....	42
Figure 29: Total pressure contours for configuration 6, no injection.....	42
Figure 30: Total temperature contours for Configuration 6, no injection.....	42
Figure 31: Comparison of experimental and computational nozzle performance, configuration 7,	
2.8% injection.....	44
Figure 32: Comparison of PAB3D and Fluent wall pressures for configuration 7.....	46
Figure 33: Velocity vectors at x = 1.1 inch. Configuration 7, NPR4, 2.8% injection.....	46
Figure 34: Mach contours for Configuration 7, 2.8% injection.....	47
Figure 35: Static pressure contours for Configuration 7, 2.8% injection.....	47
Figure 36: Total pressure contours for Configuration 7, 2.8% injection.....	48
Figure 37: Total temperature contours for Configuration 7, 2.8% injection.....	48
Figure 38: Computational nozzle performance for configuration 8,9,and 10. 2.8% injection.....	50
Figure 39: wall pressures for configuration 7-10, NPR=4 , 2.8% injection.....	51
Figure 40:Mach contours for Configuration 8-10, 4% Injection.....	52

Figure 41: Static contours for Configuration 8-10, 4% Injection.....53

Figure 42: Total pressure contours for Configuration 8-10, 4% Injection.....54

Figure 43: Total temperature contours for Configuration 8-10, 4% Injection.....	55
Figure 44: Computational nozzle performance for configuration 11, 12, and 13.....	58
Figure 45: wall pressures for configuration 10-13, NPR=4 , 2.8% injection.....	58
Figure 46: Mach contours for configuration 11.....	60
Figure 47:Mach contours for configuration 13, 2.8% injection.....	60
Figure 48: Mach contours for configuration 12, 2.8% injection.....	60
Figure 49: Static pressure contours for configuration 11, 2.8% injection.....	61
Figure 50:Static pressure contours for configuration 12, 2.8% injection.....	61
Figure 51:Static pressure contours for configuration 13, 2.8% injection.....	61
Figure 52: Total pressure contours for configuration 11, 2.8% injection.....	62
Figure 53: Total pressure contours for configuration 12, 2.8% injection.....	62
Figure 54:Total pressure contours for configuration 13, 2.8% injection.....	62
Figure 55: Total Temperature contours, configuration 11, 2.8% injection.....	64
Figure 56: Total Temperature contours, configuration 12, 2.8% injection.....	64
Figure 57: Total Temperature contours, configuration 13, 2.8% injection.....	64
Figure 58: Comparison of configurations 7 through 13. 2.8% injection.....	65

List of Tables

Table 1: Balance Accuracy for 2D and 3D experimental models. ^{5,17}	14
Table 2: Geometry definitions for configurations investigated.....	24
Table 3: Comparison of computational results with PAB3D for configurations 4 and 5.....	39
Table 4: Results from Grid Generation Study.....	39
Table 5: Results from Grid generation study. Configuration 8, NPR 4, 2.8% injection.....	56
Table 6: Grid generation study results, configuration 11, NPR4, 2.8% injection.....	63

Nomenclature

- 2D = 2 Dimensional
- Ae = Exit area, in²
- At = Upstream throat area, in²
- CFD = Computational fluid dynamics
- $C_{f, sys}$ = System thrust ratio, $\frac{F_R}{F_{i,p} + F_{i,s} + F_{i,t}}$
- $C_{d,p}$ = System discharge coefficient, $\frac{w_s + w_p + w_t}{w_i}$
- D1 = Diameter of upstream throat, in (see Figure 9 and Table 2)
- D2 = Diameter of downstream throat, in (see Figure 9 and Table 2)
- DTN = Dual throat nozzle
- F_A = Axial Force, lb
- F_{i,p} = Ideal isentropic thrust of primary nozzle, lb
- F_{i,s} = Ideal isentropic thrust of secondary injection flow, lb
- F_{i,t} = Ideal isentropic thrust of tertiary injection flow, lb
- F_{lift,q} = Lift force for phase q, lb
- F_N = Normal Force, lb
- F_q = External body force for phase q, lb
- F_R = $\sqrt{F_A^2 + F_N^2 + F_S^2}$, lb
- F_S = Side Force, lb
- F_{vm,q} = Virtual mass force for phase q, lb
- FTV = Fluidic thrust vectoring
- g = acceleration due to gravity, ft/s²
- h_{pq} = interphase enthalpy between p and q phase, energy/mass
- h_q = Specific enthalpy of phase q, energy/mass
- h_{qp} = interphase enthalpy between q and p phase, energy/mass

k_{pq} = Interphase momentum exchange coefficient between p to q phase, dimensionless

L = Length of primary cavity, in (see Figure 9 and Table 2)

m_{pq} = Mass transfer from p to q phase, lb/s

m_{qp} = Mass transfer from q to p phase, lb/s

MTV = Mechanical thrust vectoring

NPR = Nozzle pressure ratio, $\frac{P_{p,j}}{P_a}$

NPR_D = Design nozzle pressure ratio

p = pressure, psi

P_a = Atmospheric pressure, psi

P_e = Nozzle exit pressure, psi

P_∞ = Freestream pressure, psi

$P_{t,j}$ = Total pressure of primary jet, psi

$P_{t,si}$ = Total pressure of secondary injection, psi

$P_{t,ti}$ = Total pressure of tertiary injection, psi

Q_p = Intensity of heat exchange between p and q phase, btu/ft²-h

q_q = Heat flux of phase q, btu/ft²-h

SPR = Secondary pressure ratio, $\frac{P_{s,j}}{P_a}$

S_q = Total entropy, Btu/lb mol-°F

SVC = Shock vector control

TPR = Tertiary pressure ratio, $\frac{P_{t,j}}{P_a}$

$T_{t,j}$ = Total temperature of primary jet, °F

$T_{t,si}$ = Total temperature of secondary injection, °F

$T_{t,ti}$ = Total temperature of tertiary injection, °F

u_q = Shear viscosity, lb/ft-s

v_p = Velocity of phase p, ft/s

v_q = Velocity of phase q, ft/s

v_{pq} = interphase velocity from p to q phase, ft/s

v_{qp} = interphase velocity from q to p phase, ft/s

w_p = Measured weight flow rate of primary jet, lb/sec

- $w_{i,p}$ = ideal weight flow rate of primary jet, lb/sec
 w_s = Measured weight flow rate of secondary jet, lb/sec
 w_t = Measured weight flow rate of tertiary jet, lb/sec
 α_q = Thermal diffusivity, ft²/s
 γ = Ratio of specific heat, Dimensionless
 δ_p = Resultant thrust vector angle $\tan^{-1}\left(\frac{F_N}{F_A}\right)$, deg
 ε = Turbulent dissipation rate, ft²/s³
 η = Thrust vectoring efficiency, $\frac{\delta}{(w_s + w_t / (w_s + w_t + w_p)) * 100}$, deg/% injection
 θ_1 = Upstream divergent cavity ramp angle, deg (see Figure 9 and Table 2)
 θ_2 = Downstream convergent cavity ramp angle, deg (see Figure 9 and Table 2)
 ρ_q = Density of phase q, lbm/ft³
 ρ_{rq} = Phase reference density, lbm/ft³
 τ_q = Stress strain for tensor for qth phase, lbf/ft²
 ϕ_1 = Secondary injection angle, degree (see Figure 10 and Table 2)
 ϕ_2 = Tertiary injection angle, degree (see Figure 10 and Table 2)

I. Introduction

While designing a fighter aircraft, improving the agility, maneuverability, and survivability of the aircraft are key to a successful design. Thrust vectoring can dramatically increase these design parameters². This method is also used to help satisfy take-off and landing requirements. In addition, this method can reduce cruise trim drag by providing control power for trimming³. Due to the engine forces being less dependent on the external flow, thrust vectoring is the most efficient way for increasing lift and drag upon stall of control surfaces⁴. This method is also proven to increase fuel efficiency since control surfaces require more thrust. There are two ways to accomplish thrust vectoring, mechanical and fluidic. Mechanical thrust vectoring (MTV) can be achieved using movable flaps or adjustable nozzles. Mechanical thrust vectoring has been used on different fighter aircraft such as the F/A-18 HARV, F-22 Raptor, and Eurofighter Typhoon. The F-22 Raptor, with its 2 dimensional convergent divergent nozzle, can achieve thrust vectoring angles up to 20°. MTVs use actuated hardware to redirect the exhaust flow off-axis. Although, the current MTV systems used on aircrafts are successful for their specified mission requirements, they can be heavy, complex, difficult to integrate, expensive to maintain, and aerodynamically inefficient⁵. The two types of mechanical thrust vectors are demonstrated in Figure 1 and Figure 2. 30% of the F-22 Engine, shown in Figure 1, is devoted to parts for MTV mechanisms of the system needed for its specific flight requirements⁶. Figure 2



Figure 1: Pratt and Whitney F-199-PW-100⁶



Figure 2: Eurojet EJ200⁶

demonstrates the adjustable nozzle used on Eurojet EJ200. One can observe the manufacturing difficulties by glancing at such engine. Due to these complications, fixed geometry fluidic thrust vectoring (FTV) systems have become more favorable over MTV systems.

Unlike mechanical thrust vectors, FTV nozzles use a secondary air stream to manipulate or control the primary exhaust flow, therefore redirecting the flow at or before exit conditions². The primary FTV methods are shock vector control, throat shifting, counterflow, and combined methods². Fluidic shock vector control (SVC) manipulates the flow by injecting a secondary air stream at the divergent section of the

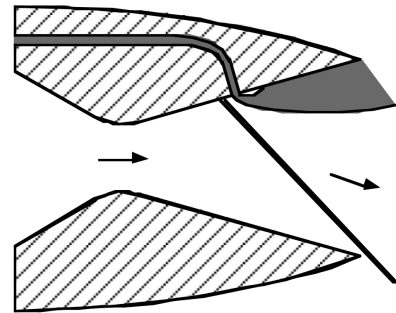
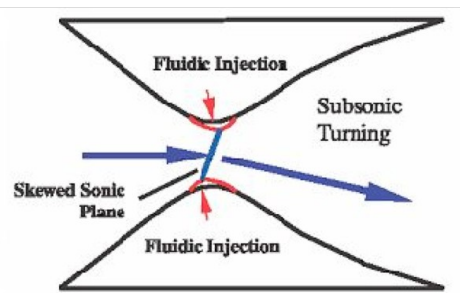


Figure 3: Shock Vector Control⁷

nozzle shown in Figure 3. This injection acts as a pressure ramp and turns the flow supersonically⁶. The shock vector method offers thrust vector angle such as 3.3°/% flow rate injection; however, this method often reduces the system thrust ratio. SVC method has thrust ratio ranges of 0.86 to 0.94^{5,7}.

Throat shifting generates higher thrust vectoring efficiencies compared to other FTV methods. The throat shifting method injects the flow at or near the throat (Figure 4), turning the flow before supersonic speeds. This method manipulates the flow prior to its supersonic stages, thus not significantly affecting the system thrust ratio. The throat shifting method provides impressive thrust ratios of .94 to .98; however, it only



provides vector efficiencies up to 2°/° injection. Although, this method can only provide for mild maneuver adjustments, work done by NASA Langley research center suggests that this is a promising method in the future due to its high thrust ratios⁸.

Unlike the throat shifting and SVC method, the counter flow method provides thrust vectoring using secondary suction. Suction is applied to one side of the jet, creating reverse flow at the wall of the suction collar, therefore mixing the shear layers, reducing the pressure, and redirecting the flow. This method was first reported by Strykowski and

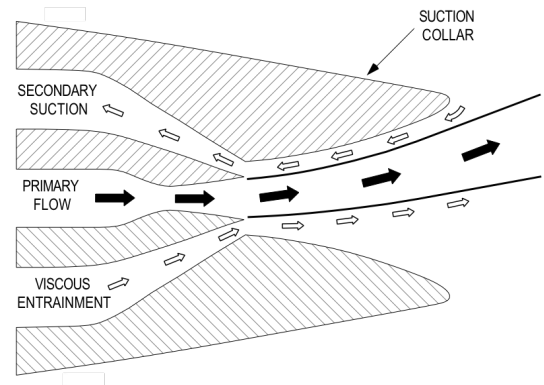


Figure 5: Counterflow Thrust Vectoring⁵

Krothapali⁵ and is shown in Figure 5. This method can provide vectoring angles up to 15° and thrust ratios of 0.92 to 0.97 with little secondary suction⁵. Even though, this method provides great vectoring angles, it brings up issues such as secondary suction source and hysteresis effects^{2,7}.

The method being investigated in this study is a combined method. The Aerospace Vehicle System Technology office at NASA Langley has been investigating this combination method experimentally and computationally for over 10 years^{2,3,9}. The computational study was done using a structured, unsteady CFD code, PAB3D. The studies implement the throat shifting method at the upstream throat of a dual throat nozzle (DTN) (also known as recessed cavity nozzle) shown in Figure 6. Even though a DTN cannot provide thrust vectoring on its own, it can provide thrust ratios of 0.94 to 0.96 with vectoring

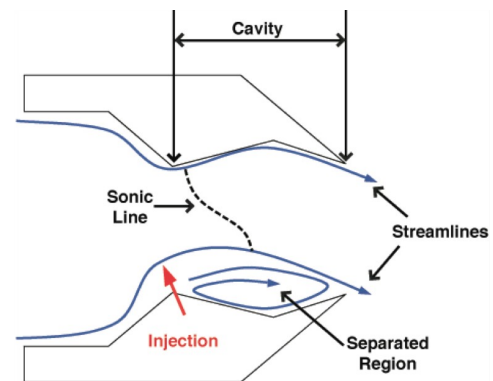


Figure 6: Dual Throat Nozzle with fluidic injection at upstream throat³

efficiencies from 3.8° to 5.2°/° injection. In this study, steady state cases of the NASA Langley studies for the DTNs were concluded and they were compared against experimental and computational unsteady results to validate the capability of ANSYS Fluent solving internal flow

of DTN. Later, the study will focus on combined methods that will include a tertiary injection in addition to the secondary injections. This tertiary injection will focus on different angles of external injections and exit line injections.

II. Experimental Method

The experimental results used to benchmark the computational outcome achieved in this paper were completed using the NASA Langley's Jet Exit Test Facility¹⁰. The tests were conducted and published by the aerodynamics branch at NASA Langley^{3,11}. This facility is an indoor reduced-scale pressurized-air test stand, which includes a dual-flow propulsion system used for high pressure and high internal flow tests. This system provides high-pressure air delivered from a 5000-psi compressor station, which is reduced to feed two 1800-psi air lines used for the primary and the secondary flow of the nozzle. The photographs in Figure 8 and Figure 7 demonstrate the 2D and 3D nozzles at the facility. This wind tunnels can provide up to 25 lb/sec flow rates and includes a steam heat exchanger to maintain the secondary total temperature at temperatures around 75 °F. The rigs also include a high-pressure hose used to connect to a remote control for activating the secondary injection. The next two sections will provide a summary of the dual-flow propulsion system, model hardware, and accuracy of the different instruments used during this experiment.

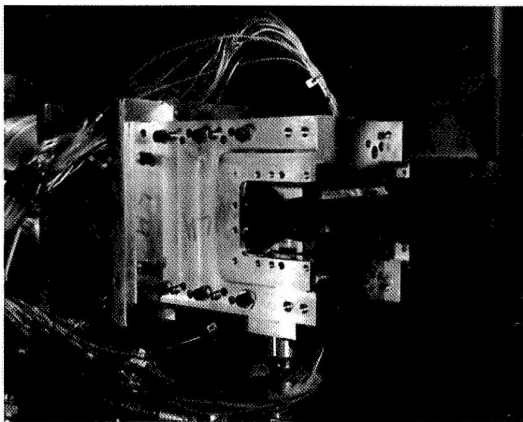


Figure 8: NASA Langley Research Center 2D DTN Fluidic thrust nozzle installed in the Jet Exit Test Facility¹¹

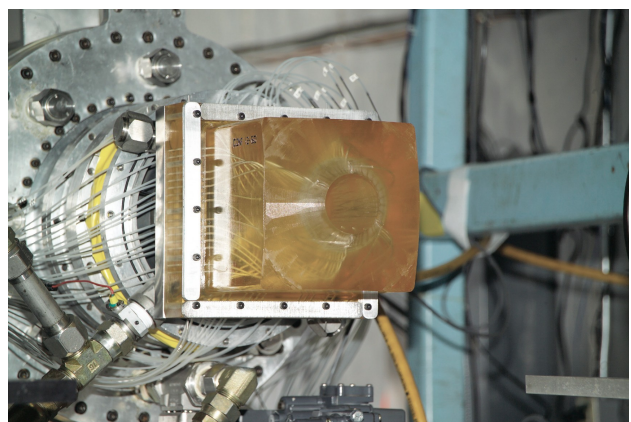


Figure 7: NSASA Langley Research Center axisymmetric DTN installed in the Jet Exit Test Facility³

A. Axisymmetric Model

The Forces and the moments on this axisymmetric nozzle were measured using a six-component strain gauge balance and the maximum capacities of the measurements are provided in Table 1. This model was equipped with 56 surface static pressure taps that were placed on the centerline of the upper and lower surfaces. The taps were approximately about 0.4 inch apart and they started at 0.6 inch upstream of the upstream nozzle throat, leading to the nozzle exit. The static pressures were measured using pressure transducers with a range of 250 psid, which was exceeding the expected pressure measurement. The accuracy of the pressure transducers are +/- 0.1 percent of full scale. The primary total pressure was obtained from the average of 8 Pitot probes installed upstream of the primary nozzle. The pressures for these probes were measured using individual pressure transducers with a range of 500 psid, with an accuracy of +/- 0.1 percent of full scale. The primary jet total temperature was computed using 2 thermocouples mounted in the same section as the pressure transducers, with an accuracy of +/- 4°F. The secondary pressure and temperatures were also calculated using similar instrumentations as the 2D case in the next section; however, they will not be discussed in this report since the solutions including the secondary injections for the 3D models are not used. These details are included in reference 3. The geometry of this axisymmetric nozzle with no secondary injection is provided in Figure 9.

B. 2 Dimensional Results

The forces and the moments on this dual throat nozzle were also measured using a six-component strain gauge balance and the maximum capacities of the measurements are the same as the axisymmetric nozzle in pervious section. These maximum capacities are provided in Table

1. A total of 68 surface static pressure tabs were installed on the centerline of this nozzle. The pitots were spaced 0.19 inch apart and they started at 0.2 inch upstream of the primary nozzle leading to the exit of the nozzle. The static pressures were measured using electronic pressure transducers rated at 100 and 250 psid depending on the expected measurements. The transducers have an accuracy of +/-0.1 percent of the full scale. The primary jet pressure was found using the average of 9 pitot probes installed within the instrumentation section upstream of the primary nozzle. These pressures were similarly measured using electronic pressure transducers rated at 250psid with an accuracy of +/- 0.1 percent full scale. The total temperature of the Primary jet was recorded using a single thermocouple mounted in the instrumentation section with an accuracy of +/- 4°F. The pressure of the secondary jet was found using a single probe in the injection plenum with a 500psid pressure transducer having an accuracy of +/- 0.1 percent full scale. The total temperature of the secondary injection was measured using a thermocouple located between the hose line feeding the compressed air and the injection block with an accuracy of +/- 2°F. Finally, the ambient air was measured using a 15psi pressure transducer with an accuracy of +/- 0.03. The geometry for this is nozzle is demonstrated in Figure 9 and Figure 10. In addition to the dimensions provided, the geometry of the rig includes a 4 inch width.

Component	Balance Maximum	Max Error	Max error as % of Balance Maximum
Normal	800 lbs	0.56 lbs	0.07
Axial	12000lbs	2.38 lbs	0.2
Pitch	12000 in-lbs	17.64 in-lbs	0.15
Roll	1000 in-lbs	1.63 in-lbs	0.16
Yaw	12000 in-lbs	26.07 in-lbs	0.22
Side	800 lbs	0.47 lbs	0.06

Table 1: Balance Accuracy for 2D and 3D experimental models.^{3,11}

II. Computational Method

ANSYS FLUENT¹² is a commercially available CFD code used for this study. This software is known to be one of the more popular CFD codes used in the industry. Unlike codes developed for specific studies such as PAB3D, OVERFLOW, and VULCAN, ANSYS Fluent is known to be a general code. This CFD software is also known for its uncomplicated interface compared to most internal codes developed by other companies. One advantage of this codes is the ability to bring in a 2 dimensional mesh used for 2D and 2D axisymmetric cases. Codes developed by NASA such as PAB3D, OVERFLOW, and VULCAN require a thickness for these cases. This requires more time spent on grid generation, setting boundary layers, and increases computational time due to the extra cells.

This software has been tested and predicted accurate results for convergent divergent nozzles with secondary injections, but there are no publications on dual throat nozzles for this code. A total of 24 different cases have been computed in this study to predict the accuracy of the code with DTNs. The geometry and the boundary conditions in this study were acquired from past NASA Langley papers found in references 1-3, 9, and 11. In this study, different axisymmetric and 2D cases are compared with experimental results. Tertiary injections were then investigated for 2 dimensional geometries following the validation of the CFD code for this complex geometry.

A. Governing equations

ANSYS Fluent's provides computational solutions, using the Navier stokes equations. This includes the conservation equations of mass, momentum, energy, and also the equation of

state. Equations 1-3 demonstrate the conservation of mass, momentum, and energy solve by ANSYS Fluent:

$$\frac{\partial}{\partial t} (\alpha \rho) + \nabla \cdot (\alpha \rho \mathbf{v}) = \sum_{p=1}^n (m_{pq} - m_{qp}) \quad (1)$$

$$\frac{\partial}{\partial t} (\alpha \rho \mathbf{v}) + \nabla \cdot (\alpha \rho \mathbf{v} \mathbf{v}) = -\alpha \nabla p + \nabla \cdot \boldsymbol{\tau} + \alpha \rho \mathbf{g} + \sum_{p=1}^n (K_{pq} (\mathbf{v}_p - \mathbf{v}_q) + m_{pq} \mathbf{v}_{pq} - m_{qp} \mathbf{v}_{qp}) + (F_q + F_{lift,q} + F_{vm,q}) \quad (2)$$

$$\frac{\partial}{\partial t} (\alpha \rho h) + \nabla \cdot (\alpha \rho \mathbf{v} h) = \alpha \frac{\partial p}{\partial t} + \nabla \cdot \mathbf{q} + S_q + \sum_{p=1}^n (Q_{pq} + m_{pq} h_{pq} - m_{qp} h_{qp}) \quad (3)$$

More information on Navier Stokes equations, and the variables used in equations 1-3 is provided in reference 9.

These equations can be solved using Roes or AUSM schemes for first, second, or third order. Also these schemes can be solved implicitly or explicitly. One disadvantage of Fluent is that it does not support Van leer's scheme. Typically the explicit formulation is used for Roe's flux-difference splitting scheme and Implicit is used for Van Leer's flux vector-splitting scheme¹³. Van leer's and Roe's scheme were used in previous papers previous papers from

NASA Langly¹, but due to the limitations of Fluent, Roes scheme was used to implicitly to solve the entire problem.

B. Solver Setting, ANSYS Fluent

There are two different solvers within Fluent, pressure based and density based. The pressure-based solver is normally used for lower speeds and the density-based solver is used for higher speeds and is recommended for compressible flow problems. Therefore, a steady state density-based solver was used for this study. Unsteady Navier stokes equations have been used in most previous research, but due to hardware limitation, a steady state solver was used in this study to reduce computational time. To confirm the results 3 different unsteady state solutions were computed and compared to steady state solutions. These solutions will be discussed in the later section. The unsteady solutions were stopped after $1e^{-2}$ seconds, which corresponds to less than 0.5° of change in the thrust vectoring angle after several thousand iterations. It is important to note that since the steady state solver was used for this unsteady problem, it is needed for the convergence plot to steady for all variables. This is about 20 thousand iteration for all configurations with the current grid density.

Fluent has many different viscous models including, Spalart-Allmaras (1 equation), k-epsilon (2 equations), k-omega (2 equations), and Transition Sheer Stress Transport (4 equations) with Spalart Allmaras being the least and Transition sheer stress transport being the most accurate. More information is given within the ANSYS Fluent 13.0 manual¹². The 2-equation realizable k-epsilon model, with the energy equation activated was used in this study due to the accuracy of the k-epsilon model for internal nozzle performance described in previous papers^{3,5,7,9}. The realizable model is more advanced than the standard k-epsilon. This model can provide accurate solutions for all attached and very little separated flow using the standard wall function. This model was used on the first 6 configurations of this paper. After investigation, it was realized that the standard wall function should be restricted to non-separated flow. Therefore, the non-equilibrium wall function was used for configurations 7-13. Solutions from

4-equation SST model were also computed and compared to the k-epsilon model for 3 different nozzle pressure ratios (NPR). The results for these equations take much longer to achieve and the percentage differences of the results were less than 1. Thus, the k-epsilon model with 2nd order flow was used for the remainder of the study. In the material section of Fluent, ideal gas was selected for the density properties and Sutherland's law was used for the viscosity of the model. Fluent automatically activates the energy equation while ideal gas is selected since the energy equation is required for compressible flow problems. As stated previously, Roe's upwind scheme was solve implicitly for the entire solution since Van Leer's scheme is not an option for Fluent.

C. Performance calculation

The performance characteristics were achieved using Fluent's reports and equations from previous work done^{2,3,9,12}. Fluent report's can provide the exit conditions of the nozzle required to calculate the thrust ratios. Previous research provides the nozzle geometry along with NPRs and the percentage flow rate of the secondary flow with respect to the primary flow. The NPR is the ratio of jet primary flow total pressure, $p_{t,j}$ to the freestream pressure, P_∞ and the secondary flow is determined by a given percentage of the primary mass flow rate or secondary pressure ratio (SPR). SPR is the ratio of the secondary total pressure, $p_{t,si}$ to the freestream pressure. Since previous paper do not provide the pressure and temperature of the secondary nozzle, SPRs of 1.5 was used for all cases. Later in the study, it was discovered that this SPR provides a 2.8% injection as a replacement for 3% used in previous studies. However, this injection was not changed since the results were comparable. The temperature of the nozzle was calculated using the isentropic equation provided by equation (4). $\gamma = 1.4$ was used for air at standard condition¹⁵.

$$\left(\frac{p_2}{p_1}\right)^{\frac{\gamma-1}{\gamma}} = \frac{\rho_2}{\rho_1} = \frac{T_2}{T_1} \quad (4)$$

The results were compared to experimental results using a system thrust ratio ($C_{f, \text{sys}}$), System discharge ratio ($C_{d,p}$), thrust vectoring angles (δ_p), and thrust vectoring efficiency (η) of the model. $C_{f, \text{sys}}$ is the ratio of the resultant force achieved from computational results to sum of the ideal isotropic thrust of the primary and secondary flow¹⁴:

$$\frac{F_R}{F_{i,p} + F_{i,s} + F_{i,t}} \quad (5)$$

The resultant forces are calculated from using the thrust equation given in reference 15:

$$F_R = mV_e + (P_e + P_a)A_e \quad (6)$$

and the ideal isentropic thrust for the primary jet, secondary, and tertiary injections are specified as¹⁴:

$$F_{i,p} = \sqrt{\frac{2\gamma R}{\gamma-1}} w_p \sqrt{T_{t,p} \left(1 - \frac{P_{t,j}}{P_a}\right)^{\frac{\gamma-1}{\gamma}}} \quad (7)$$

$$F_{i,s} = \sqrt{\frac{2\gamma R}{\gamma-1}} w_s \sqrt{T_{t,si} \left(1 - \frac{P_{t,si}}{P_a}\right)^{\frac{\gamma-1}{\gamma}}} \quad (8)$$

$$F_{i,t} = \sqrt{\frac{2\gamma R}{\gamma-1}} w_t \sqrt{T_{t,ti} \left(1 - \frac{P_{t,ti}}{P_a}\right)^{\frac{\gamma-1}{\gamma}}} \quad (9)$$

Where w_p is the weighted mass flow rate and g is the gravitational force.

The discharge ratio is defined as¹⁴:

$$C_{d,p} = \frac{w_s + w_p + w_t}{w} \quad (10)$$

The pitch thrust vector angle, which is defined in degrees, can simply be found using the law of tangents can be expressed as¹⁴:

$$\delta_p = \tan^{-1}\left(\frac{F_N}{F_A}\right) \quad (11)$$

Finally, the thrust vectoring efficiency, which is defined in degrees per percentage injections can be expressed as¹⁴:

$$\eta = \frac{\delta}{(w_s + w_t / (w_s + w_t + w_p)) * 100} \quad (12)$$

All single injected results, except the results for thrust vectoring efficiency, will be compared to doubly injected results for comparison in later sections. These results cannot be compared due to the difference of the injections being applied for these two different scenarios. This will be discussed in section III 2. The equations for the primary and secondary flows are acquired from references provided and the third injection was simply added to the equations. The secondary and tertiary variables are to be removed for nozzles with single injection or no injections.

Wolfram Mathematica was used for calculations of the results. Mathematica is a commercially available software, much like Matlab, that can be used to for programming. An

advantage of this software is the clear formatting that it offers. This makes writing and reading the equations much simpler. A code was developed to calculate equations 1-12 using Fluent's solutions. This code provides the system thrust ratio, thrust vectoring angle, thrust efficiency, and discharge ratio as end results. The calculations are provided in the Appendix of this report.

D. Nozzle Geometry

The geometry for previous studies is to augment the thrust vectoring efficiencies. The geometries offers impressive thrust vectoring angles and nozzle performance by injecting the primary flow at the upstream throat area and manipulating flow separation in the recessed cavity². A sketch of the nozzle is shown in Figure 9 and Figure 10. All edges were rounded for the configuration to reduce skewed cells. The geometry variables of the nozzle shown in these figures are provided in Table 2. The geometries in this study include a tertiary injection at the exit line and post exit of the nozzle in addition to the secondary injection. This length, L_2 is located from the cavity to the edge of the tertiary injection. The recessed cavity (L) is located between the between the upstream throat and the downstream throat areas. The secondary injection (\emptyset_1) is located at the upstream minimum area and the tertiary injection (\emptyset_2) is located at the downstream minimum area. Previous studies include variables such as cavity divergent angle (θ_1), cavity convergence angle (θ_2), upstream height (D_1), and downstream height (D_2). However, this study will focus on the same nozzle geometry from reference 11 and adds a tertiary injection at the downstream throat. The current 2D geometry (Configuration 7) being studies is selected due to its high performance vectoring efficiencies in past studies done by NASA Langly¹ and this study will concentrate on improving this nozzle with a tertiary injection.

Configurations 1-3 were used to for benchmarking axisymmetric cases with no secondary injections. The objective of this study in early stages was to improve the thrust vectoring on a 3D DTN nozzle. After generation of the 3D grid, it was determined that the system used to run Fluent was much less powerful than expected. This was due to using a turbulent case to compute the Navier stokes equations. Turbulent computations in CFD take much longer than a laminar. Therefore, the study was then focused on 2 dimensional nozzles.

Configurations 4 and 5 were used to provide preliminary results. Configuration 4 does not include a secondary injection, but configuration 5 includes a 90° injection at the upstream throat. This configuration was used to determine if ANSYS Fluent could provide converged solutions for a DTN nozzle with a secondary injection.

Configurations 6 and 7 were also used for benchmarking purposes. Configuration 6 does not include secondary or tertiary injections, but configuration 7 includes a secondary injection. The injection port diameter for this case was 0.02 inch. This high performance trust vectoring model selected from reference 1, will be used as a base to compare results including tertiary injections.

Configuration 6-8 included an external injection post exit line shown in Figure 10. These configuration includes 3 different tertiary angles (θ) and they were selected to investigate the effects of external fluidic injection on DTNs. The injection ports for this case were kept similar to the secondary injection with a diameter of 0.02 inch.

Configurations 9-11 include tertiary injections, shown in Figure 10. This injection is located at the exit line; therefore, it can be argued if this is in fact an external or internal injection. Thus, this study will refer to the cases as the exit line injection.

All geometries for this study were created using Pro Engineer Wildfire. 2 dimensional surfaces were created using Pro Engineer and iges files were saved and transferred to CadFix. CadFix is another commercially available software that can transfer iges files to .tri files. This file is required by Gridpro for transfer of CAD files. These surfaces were then used in Gridpro to create 2 dimensional line codes. This is a very lengthy process completed for every configuration; however, there are other methods to transfer CAD files to Gridpro files that can be less time consuming.

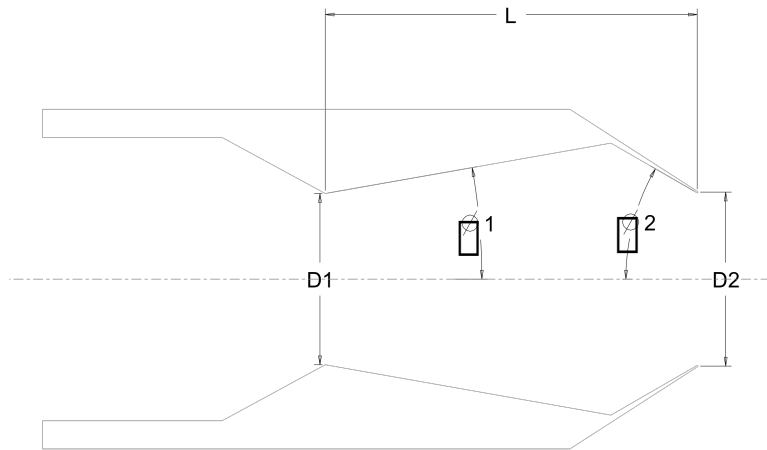


Figure 9: Geometry for DTN nozzle with no injections. Figure not to scale.

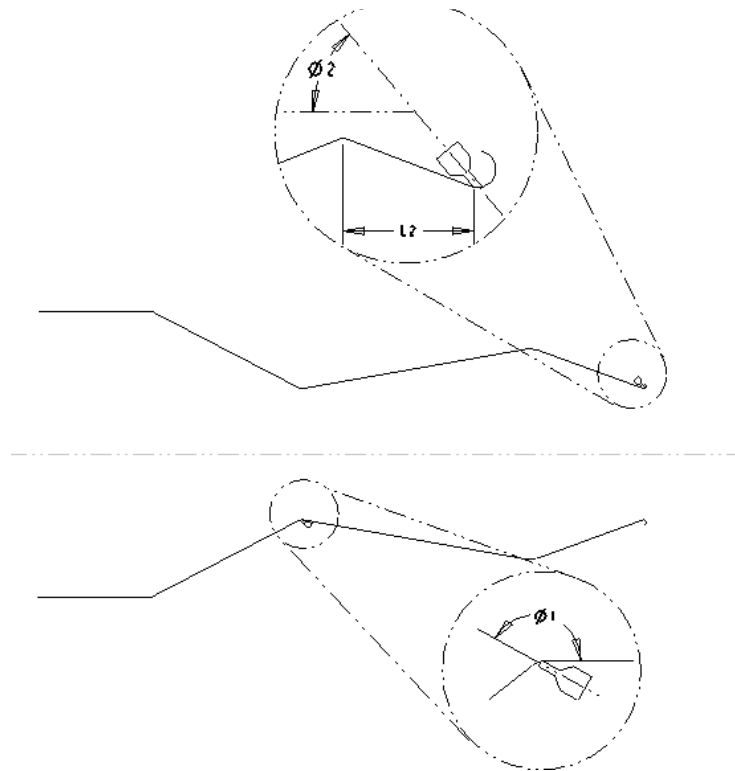


Figure 10: Geometry of DTN nozzle with injections. Figure not to scale.

Configuration	Ø 1	Ø 2	L	L2	D1	D2	ϕ1	ϕ2
1 (axisymmetric)	10	30	5.26	-	2.42	2.42	0°	0°
2 (axisymmetric)	10	20	5.26	-	2.42	2.94	0°	0°
3 (axisymmetric)	10	11	5.26	-	2.42	3.36	0°	0°
4 (2D)	10	20	1	-	1.15	1.15	0°	0°
5 (2D)	10	20	1	-	1.15	1.15	90°	0°
6 (2D)	10	20	3	-	1.15	1.15	0°	0°
7 (2D)	10	20	3	-	1.15	1.15	150°	0°
8 (2D)	10	20	3	0.97	1.15	1.15	150°	50°
9 (2D)	10	20	3	0.97	1.15	1.15	150°	40°
10 (2D)	10	20	3	0.97	1.15	1.15	150°	30°
11 (2D)	10	20	3	0.99	1.15	1.15	150°	70°
12 (2D)	10	20	3	0.99	1.15	1.15	150°	50°
13 (2D)	10	20	3	0.99	1.15	1.15	150°	40°

Table 2: Geometry definitions for configurations investigated (Dimension are provided in inches).

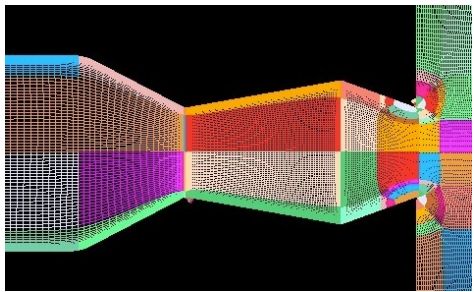
E. Grid Generation

The software used for grid generation in this study was GridPro¹⁶. This is a topology-based software that can decrease the time spent on the gridding process dramatically. It provides multi-block structured grids and it can implement a rap around topology around the exit of the nozzle, therefore creating noticeably less skewed cells as shown in Figure 11b. This tends to provide better results, helps with the convergence, and reduces the computational time of the solution. The grid in this study was transferred using only one block, as Fluent does not support multi block calculations. For configurations 1 to 3 represented in Table 2, the far-field boundaries were located 4 cavity length downstream and 2 cavity length upstream of the nozzle exit. The upper far-field conditions were located 5 cavity lengths from the center axis. The far- field boundaries were extended for configurations 4 and 5 to: 8 cavity lengths downstream, 6 cavity lengths upstream, and 10 cavity lengths for upper and lower far-fields conditions. Finally, configuration 7 was computed with 5 cavity lengths downstream, 4 cavity length upstream, and 6 cavity lengths for upper and lower lateral far-field boundaries.

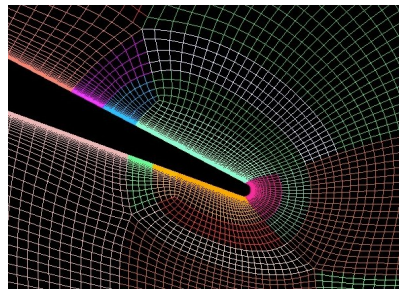
The boundaries provided for configuration 7 were then decreased by small lengths to decrease the total cells down for the study. This was mainly done to reduce the computational time for the unsteady solutions presented in later sections. The final result for the downstream boundary is 1.25 cavity lengths downstream of the exit line. The upper and lower freestream inlet is located at the nozzle exit for configurations with tertiary injections and 0.3 cavities for configuration without the tertiary injections. The upper and lower far-fields are located 1.6 cavity lengths above and below the centerline of the nozzle. Originally, the study was started with 220,000 grid cells. This reduction decreased the total grid cells to 61,000. This also lowered the computational time by 3.5 hours, resulting the solution to converge in 2.5 hours.

Later in the study, it was realized that reducing the downstream outlet boundary decreases the computational time dramatically and helps with convergence of the solution, and the computational time. With most cases in this study, Fluent's "reverse flow" warning for the outlet boundary appears for parts of the computation. Many online CFD discussions predict that this problem can be solved by extending the outlet boundary condition further from the walls; however, shorting the boundary condition is much more useful for this study. As the downstream outlet is extended, the model will experience reverse flow at the outlet boundary for a longer period of time. This is due to the unsteadiness of the solution and to help the solution converge, the outlet boundary needs to be relocated closer to the nozzle exit to prevent the reverse flow for a long period of time. The plume is predicted from the calculation of the upstream cells. Therefore, as the outlet boundary is extended further away, the reverse flow warning will stay on longer and this could provide inaccurate solution. This warning is to be ignored if on for a short period of time, but it is customary to improve the grid or boundary conditions if this warning stays on for longer periods.

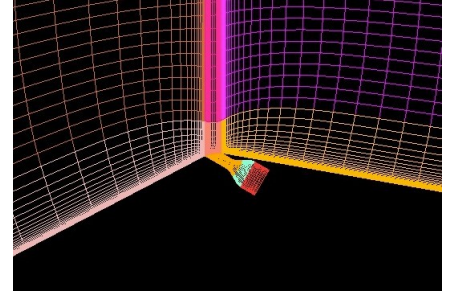
The boundary layer clustering for the main nozzle walls, used on all configurations, have a minimum value of $1.0e^{-4}$ inch with a stretching of 1.1. The secondary injection has a clustering of $1.0e^{-3}$ inch with a grid stretching of 1.1. The tertiary injection was not set for a specific boundary layer clustering; however, the grid points assigned normal to the inlet, provided a $10e^{-3}$ inch spacing for every cell in the nozzle. The grid for configurations with a secondary and tertiary injections are shown in **Figure 11**.



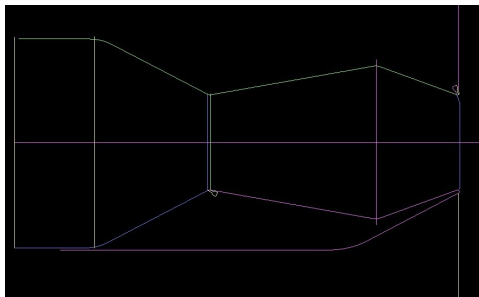
(a) Symmetry plane, configuration 13



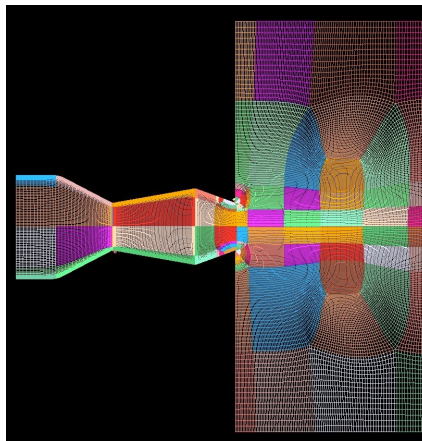
(b) Upper wall nozzle exit.
Configuration 7



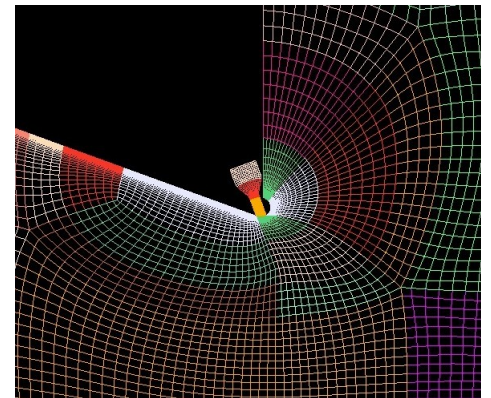
(c) Secondary injections,
configuration 13



(d) Internal surfaces, configuration 13



(e) Full grid, configuration 13



(f) Tertiary injection, configuration 13

Figure 11: Some views of computational mesh generated using GridPro.

A total of 5 internal surfaces were used during the generation of the grids. These surfaces were used to capture the geometry and provide clustering for the nozzle. The three main internal surfaces are located at the upstream throat with a clustering of $1e^{-3}$ inches, at the cavity with a clustering of $5.0e^{-3}$ inches, and post nozzle for configurations including tertiary injections. The internal surfaces can be seen from Figure 11d. The internal surface for the upstream throat provides clustering to fully capture the sonic line as well as capturing the rounded edges of the nozzle as mentioned in sections III.D. The second main internal surface located between the divergent and convergent part of nozzle is strictly included for capturing the rounded edges of the nozzle. The third main internal surface was included due to Gridpro requiring this surface for convergence. The fourth and fifth surfaces are located at the beginning of the first convergent walls and on the centerline of the nozzle. These surfaces are not required due to the surfaces having very little effects on the convergence of the nozzle, but they can be used to keep the grid points aligned at their locations.

The wrap around topology around the exit of the nozzle shown in Figure 11b was also applied for the tertiary injection configurations. It is essential to lower the amount of skewed cells while generating structured grids. This helps with the convergence of the problem and could provide more accurate results depending on how skewed the grid cells are. However, this is not always possible to do with complex geometries such as the cavity nozzle, including secondary and tertiary injections. Some cells are skewed near the secondary and tertiary injections as shown in Figure 11c and Figure 11f, but after comparing the computational results to the experimental results provided by NASA Langley, it was confirmed that the skewed cells did not affect the solutions provided by ANSYS Fluent.

Another method to lower the computational time was to use a butterfly topology downstream of the nozzle exit. This is shown in Figure 11e. This topology reduces the amount

of cells in the freestream section of the flow. More grid cells are required to capture the supersonic flow inside and downstream of the nozzle exit, but the low velocity freestream does not require such high amounts of grid cells. In fact, it is recommended to have course grid cells for subsonic flow. The butterfly method implemented here, reduces the total grid cells and helps with the convergence of the freestream flow. Therefore, decreasing the computational process of Gridpro and ANSYS Fluent.

F. Boundary conditions

1. Axisymmetric Geometry

Fluent provides many different options for defining the boundary conditions for the flow. For this study, a fixed pressure and temperature were assigned to the primary nozzle flow. For configurations 1 to 3, a pressure-far-field-boundary condition was implemented to the top and left far-field boundaries. This included a Mach number of 0.1 and a pressure of 14.6 psi. At the downstream boundary condition, a subsonic constant pressure outlet of 14.6 psi was used. This boundary automatically switches to first order extrapolation when flow reaches supersonic speeds at outlet conditions. An Axis boundary was implemented to the centerline of the axisymmetric configuration and the adiabatic wall boundary conditions were selected for the nozzle walls. Figure 12 demonstrates the boundary conditions used for configurations 1-3.

2. 2 Dimensional Geometry

Most of the boundaries used on previous configurations are implemented on the 2D nozzles, configurations 4-13. The same free stream conditions are applied to the top, bottom, and left boundaries along with the same pressure outlet boundary for the downstream outlet. As

discussed in previous sections, a mass flow rate of 2.8% is injected from the secondary injection for configuration 7 and the same mass flow rate is used for configurations 8-13. However, configurations 8-13 use both the secondary and tertiary injections. This mass flow rate was implemented with a constant pressures and temperatures for the inlets of the secondary and tertiary injection injections. The pressures and temperatures for the primary nozzle, secondary, and tertiary injections were calculated using NPRs, SPRs, and equation 4. The nozzle walls were also to be adiabatic for all 2D configurations. Figure 13 demonstrates the boundary conditions for configurations 4-13.

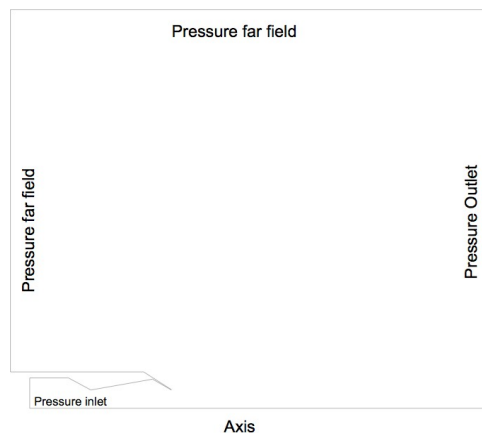
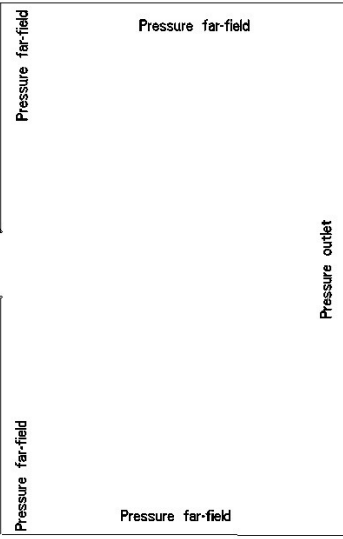
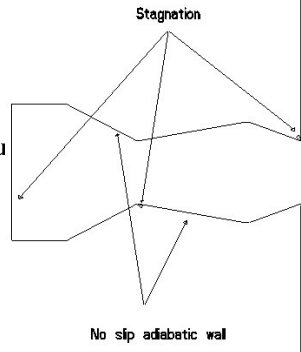


Figure 12: Boundary condition for axisymmetric nozzles. Configuration 1-3

Fig



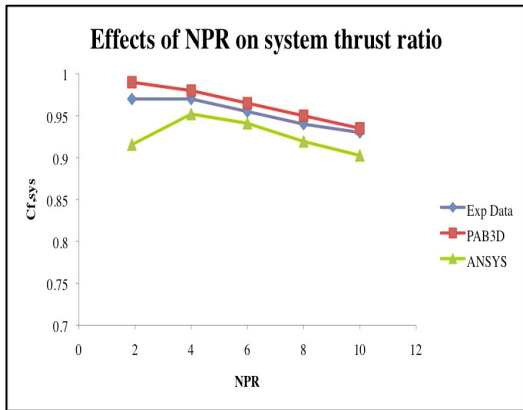
s 4-13

III. Results

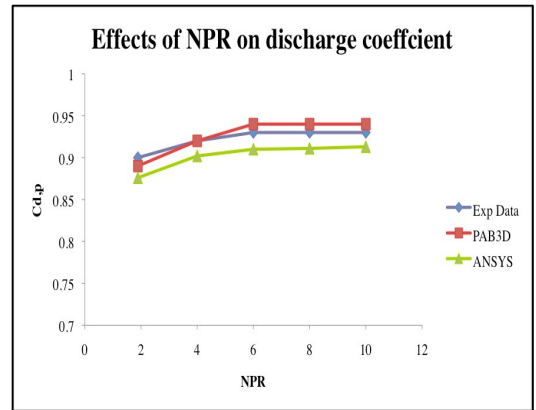
Structured grids described in previous sections and ANSYS Fluent were used to guide the analysis of the axisymmetric and 2D planar dual throat nozzles. A total of 24 simulations were computed for verification of the results: 15 axisymmetric simulations with no injections, 2 preliminary simulations with a 90° injection and without an injection, 3 2D simulations with no injection, and 4 2D simulations with a 150° fluidic injection at the upstream throat. The results were computed at NPR ranges of 1 through 10. These results will be compared with experimental and computational results from previous papers and nozzles with tertiary injections will be investigated.

A. Axisymmetric Nozzle

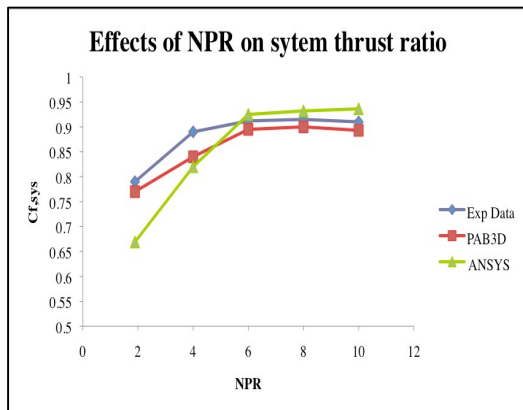
The steady state results for the system thrust ratio ($C_{f,sys}$) and the system discharge ratio ($C_{d,p}$) of configurations 1 - 3 were calculated using the equations given in section II.C. Figure 14 and Figure 15 presents the internal performance of the 3D axisymmetric cases for experimental and computational solutions. The results do not include fluidic injections and are predicted for NPRs of 3 - 10 . Initially, the results for NPRs of 1.89, 6, and 10 were achieved and it was noted that results for NPRs 6 and 10 were much more accurate. After the comparison of the resultant Mach contours, provided in Figure 16 – 18, to computation results from PAB3D³, it was confirmed that the physics of the flow was not captured for nozzle pressure ratios of 1.89. To further conform the accuracy of the results, six more cases were computed at NPRs of 4 and 8. It was then observed from Figure 14 that all solutions with NPRs of 6 and greater are accurate. This was predicted due to the steady state flow selection in ANSYS Fluent. Experimental and PAB3D results given in previous papers are unsteady, but Fluent results from current paper are



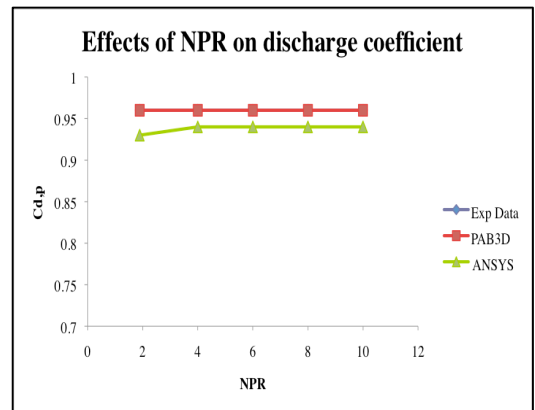
(a) Configuration 1 ($A_e/A_t = 1$)



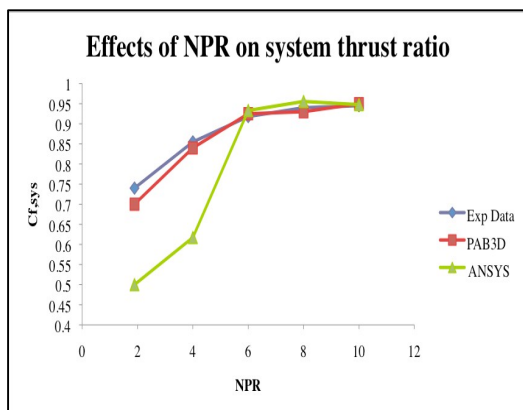
(a) Configuration 1 ($A_e/A_t = 1$)



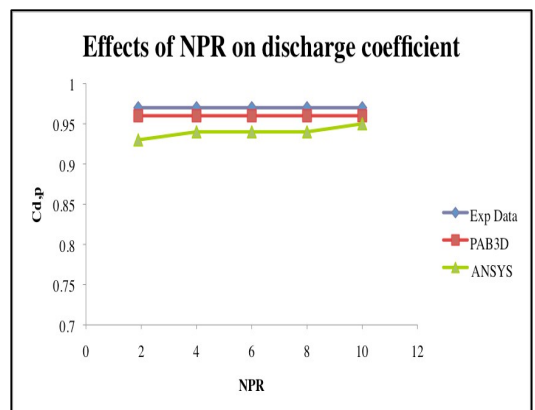
(b) Configuration 2 ($A_e/A_t = 1.47$)



(b) Configuration 2 ($A_e/A_t = 1.47$)



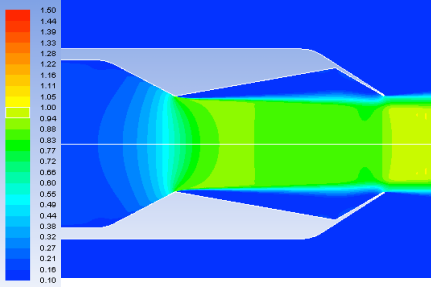
(c) Configuration 3 ($A_e/A_t = 1.93$)



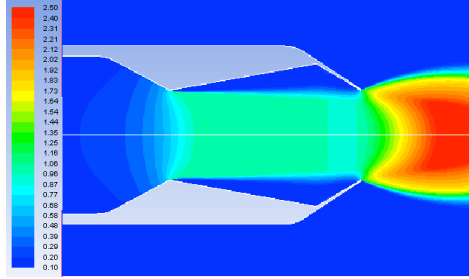
(c) Configuration 3 ($A_e/A_t = 1.93$)

Figure 14: Comparison of experimental and computational results, system thrust ratio

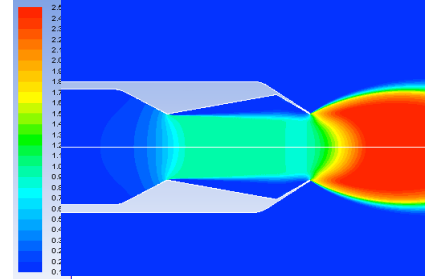
Figure 15: Comparison of experimental and computational results, discharge ratio



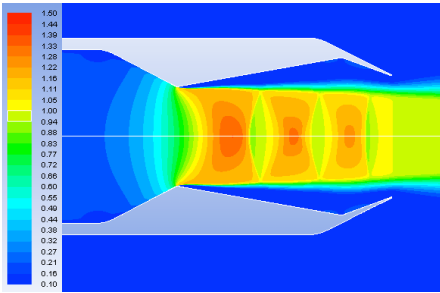
(a) Configuration 1 ($A_c/A_t = 1$)



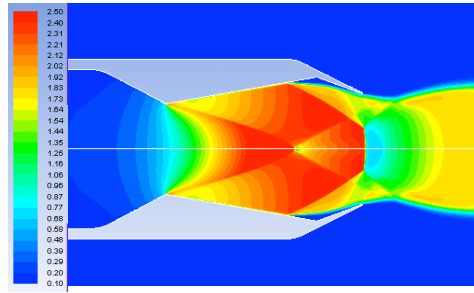
(a) Configuration 1 ($A_c/A_t = 1$)



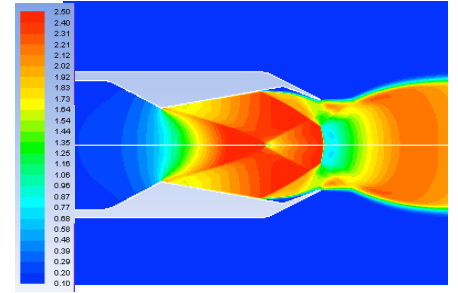
(a) Configuration 1 ($A_c/A_t = 1$)



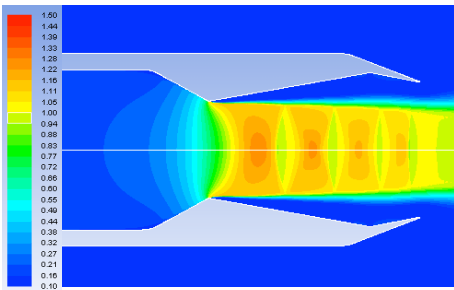
(b) Configuration 2 ($A_c/A_t = 1.47$)



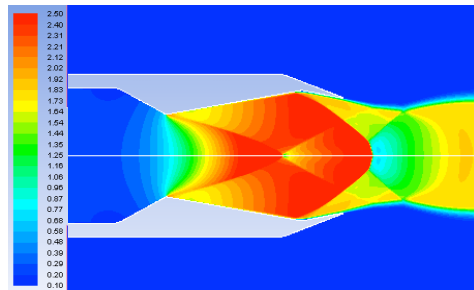
(b) Configuration 2 ($A_c/A_t = 1.47$)



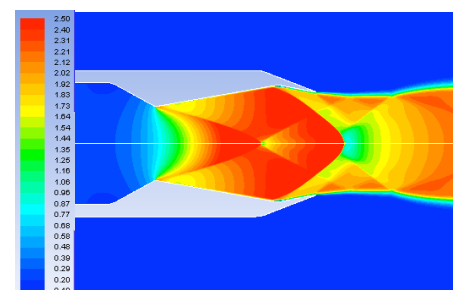
(b) Configuration 2 ($A_c/A_t = 1.47$)



(c) Configuration 3 ($A_c/A_t = 1.93$)



(c) Configuration 3 ($A_c/A_t = 1.93$)



(c) Configuration 3 ($A_c/A_t = 1.93$)

**Figure 16:Computational Mach
Contour, NPR 1.89, no injection**

**Figure 17:Computational Mach
Contour, NPR 6, no injection**

**Figure 18:Computational Mach
Contour, NPR 10, no injection**

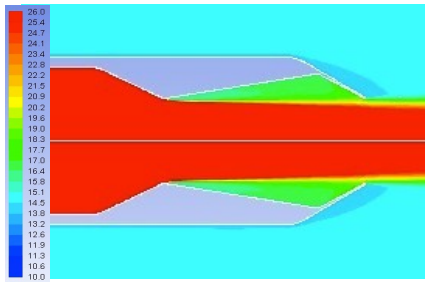
steady. Thus, it was concluded that ANSYS Fluent could provide accurate steady state results for NPRs greater than six for all configurations with the current mesh.

After further investigation of the results, it was determined that most solutions for the nozzle geometries were over expanded and the standard wall function selected from the turbulence model should be restricted to NPRs greater than the design nozzle pressure ratio (NPR_D). NPR_D is the pressure ratio of the nozzle at its ideal state. The experimental geometries used for configuration 1 – 3 have NPR_D of 1.89, 6, and 10 respectively. Therefore, all over expanded solution for configurations 1 - 3 should be inaccurate. However, Figure 14 shows that all solutions with NPRs of 6 and greater, in addition to configuration 1 at NPR of 4, were predicted accurately. This is due to the realizable k-epsilon model used for these configurations. As stated in section II.B, the realizable k-epsilon model is more advanced when compared to the standard model and although it is not recommended, it can accurately predict results for less separated flow. As the NPR increases, the flow experiences less separation. Therefore, the realizable model becomes more accurate. Figure 16b and Figure 16c can show that the flow is fully separated post upstream throat, but it becomes less separated as the NPR increases. This can also be observed from the total pressure contours shown in Figure 19 – 21. Thus, it is concluded that accurate results at NPRs 6 and greater were achieved due to the realizable k- epsilon model. No Further investigation was completed past this point since the direction of the study is changed to a 2D nozzle.

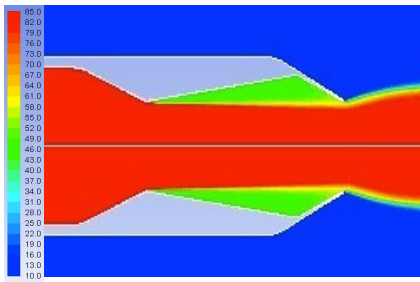
Experimental and computational results in Figure 14a, predict that the system thrust ratio peaks at NPR of 3 for area ratio of 1. The system thrust ratio is then decreased almost linearly as the NPR is increased. This decrease is due to the under expanded flow. A typical convergent nozzle peaks at the NPR_D , but the cavity in the DTN nozzle modifies this as confirmed in previous studies²⁻³. The cavity is always present to the flow even with no secondary injection and

the DTN effects penalize the system thrust ratio and discharge coefficient. This can be observed from the total pressure and total temperature contours shown in Figure 19 – 24. The total pressures shown in Figure 19a, Figure 20a, and Figure 21a do not expand around the upstream throat, resulting in total pressure loss. Due to this penalty, a DTN nozzle would be inefficient for an aircraft if thrust vectoring is not a requirement. The discharge coefficient, shown in Figure 15, is also lower from a typical convergent nozzle. This value is generally at 1 for all NPRs of a typical convergent nozzle, but it is decreased due to the effects of the DTN nozzle. The cavity nozzle experiences reverse flow at the upper and lower cavity when no secondary injection is present. This reduces the mass flow rate of the nozzle and decreases the discharge ratio.

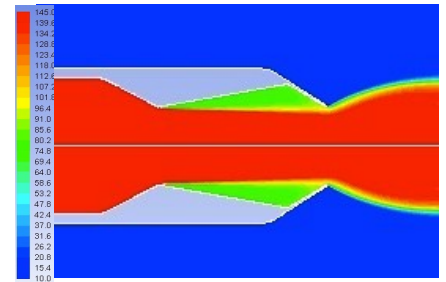
The total pressure, and total temperature contours for NPRs of 1.89, 6, and 10 with no fluidic injections are shown in Figure 21 - 24. The Mach and the total pressure contours show that the flow inside configuration 1 is subsonic inside the nozzle, but the flow is much more complex inside other configurations. This over expanded flow, including the shocks and internal losses explain why the system thrust ratio is much higher for configuration 1. As the flow crosses a shock, the total pressure and total temperature losses cannot be recovered due to the irreversibility of the flow. Therefore, it is important to avoid separation and internal shocks while designing a nozzle. The Mach and the total pressure contours can also display where the flow experiences separation for all configuration. Figure 14b and Figure 14c predict that as the NPR increases, the system thrust ratio improves for configuration 2 and 3. This can be explained from the separation shown from the Mach and total pressure contours. Since configurations 2 and 3 have higher NPR_D , the flow experiences separation at lower NPRs. Therefore, the separation of the flow, the total pressure loss, and the decreases in the total temperature lower the system thrust ratio. As the NPR increases, the flow experiences less separation and the shocks move ahead and outside the nozzle. As a result, this increases the system thrust ratio; however,



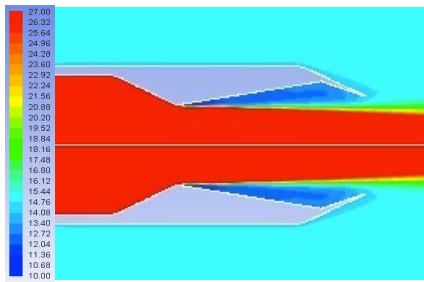
(a) Configuration 1 ($A_c/A_t = 1$)



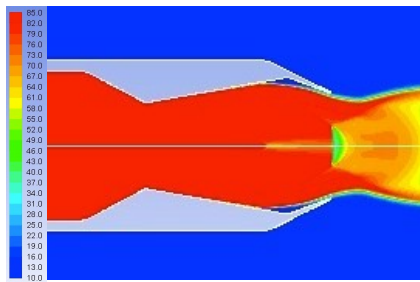
(a) Configuration 1 ($A_c/A_t = 1$)



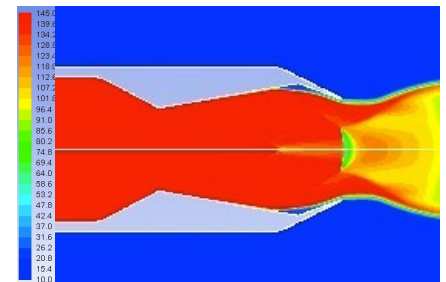
(a) Configuration 1 ($A_c/A_t = 1$)



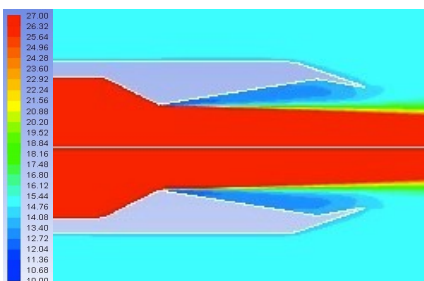
(b) Configuration 2 ($A_c/A_t = 1.47$)



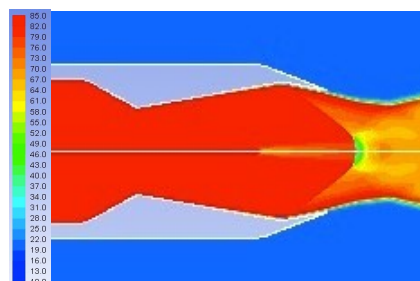
(b) Configuration 2 ($A_c/A_t = 1.47$)



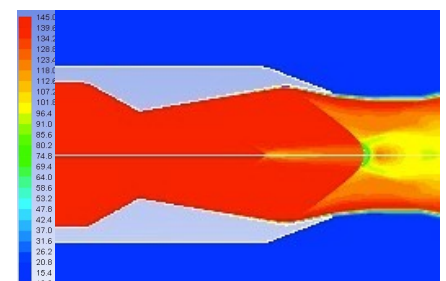
(b) Configuration 2 ($A_c/A_t = 1.47$)



(c) Configuration 3 ($A_c/A_t = 1.93$)



(c) Configuration 3 ($A_c/A_t = 1.93$)

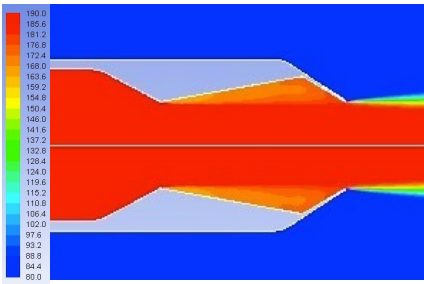


(c) Configuration 3 ($A_c/A_t = 1.93$)

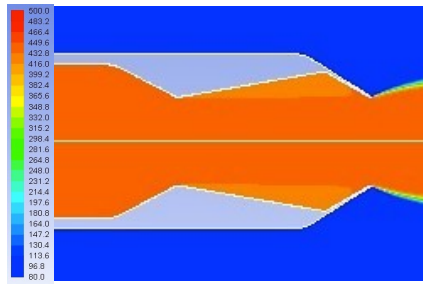
Figure 19: Total Pressure Contours, NPR 1.89, no injection

Figure 20: Total Pressure Contours, NPR 6, no injection

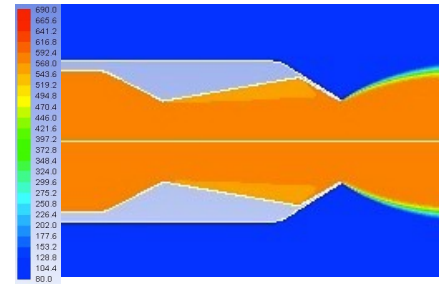
Figure 21: Total Pressure Contours, NPR 10, no injection



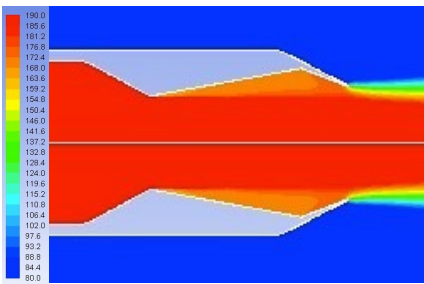
(a) Configuration 1 ($A_c/A_t = 1$)



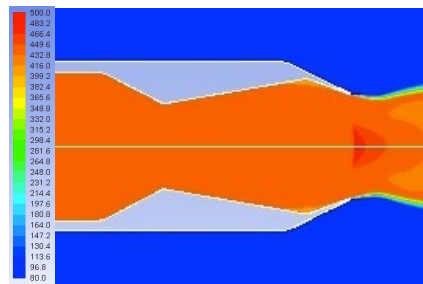
(a) Configuration 1 ($A_c/A_t = 1$)



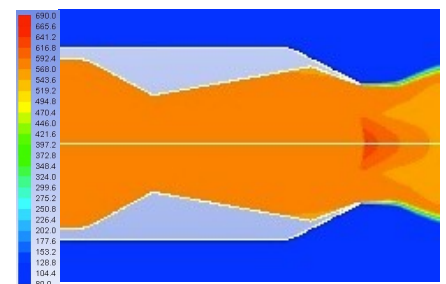
(a) Configuration 1 ($A_c/A_t = 1$)



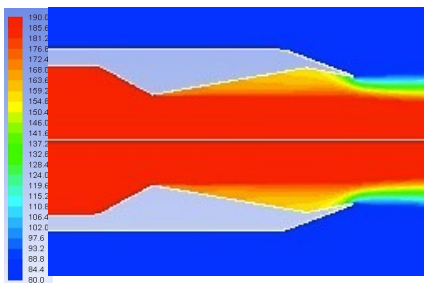
(b) Configuration 2 ($A_c/A_t = 1.47$)



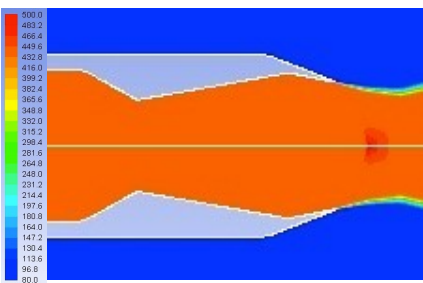
(b) Configuration 2 ($A_c/A_t = 1.47$)



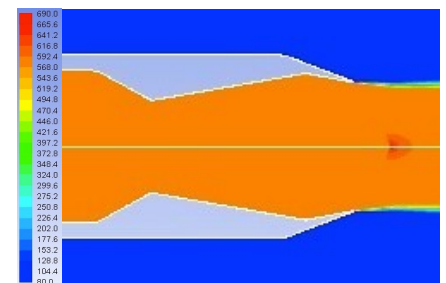
(b) Configuration 2 ($A_c/A_t = 1.47$)



(c) Configuration 3 ($A_c/A_t = 1.93$)



(c) Configuration 3 ($A_c/A_t = 1.93$)



(c) Configuration 3 ($A_c/A_t = 1.93$)

Figure 22: Total Temperature Contours, NPR 1.89, no injection

Figure 23: Total Temperature Contours, NPR 6, no injection

Figure 24: Total Temperature Contours, NPR 10, no injection

this will follow the trend of configuration 1 after reaching NPR_D since the nozzle becomes under expanded. The velocity vectors of the flow at exit conditions are also shown in Figure 25. This can show that the clustering of the grid generation by the wall does capture the full boundary layer at exit conditions. Furthermore, this proves that the inaccurate solutions for lower NPRs are not due to the grid generation.

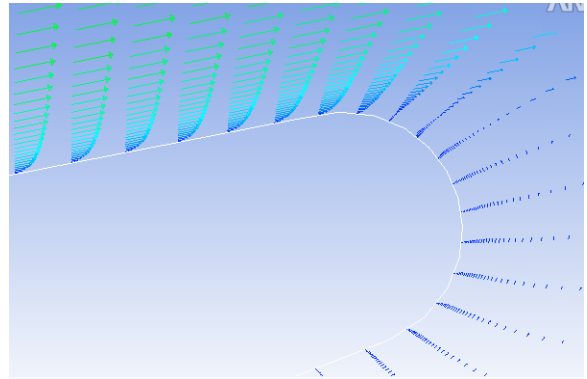
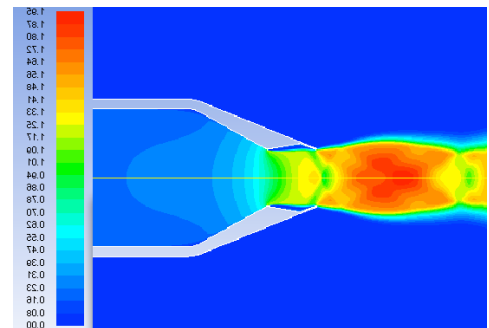


Figure 25: Velocity Magnitudes at exit, showing the capturing of boundary layer

B. Preliminary 2D Nozzle

As preliminary results, one 2D case with no injection and one 2D case with a 90° injection were computed. The Mach contours for the two different 2D configurations are shown in Figure 26a and Figure 26b and the results are presented in Table 3. The plume in this case is extremely different due to the 2D geometry and the shortening of the cavity. The NPR used for this case is 3.858. This increases the mass flow rate to about 10 times the mass flow rate of axisymmetric cases in the pervious section as the geometry is 2D. Figure 26a and Figure 26b demonstrates configurations



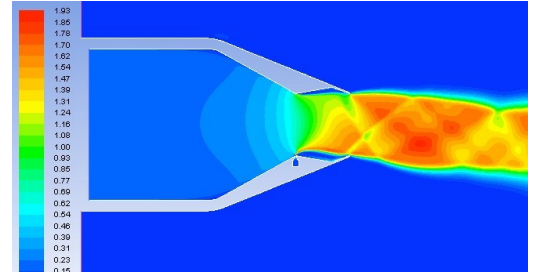
4 and 5 presented in Table 1.

There were no experimental

(a) Configuration 5 ($A_c/A_t = 1$), 90° secondary injection.

(b) Configuration 4 ($A_c/A_t = 1$). No secondary injection.

Figure 26: Mach contours for configurations 4 and 5.



results for this configuration, but the results from PAB3D and Fluent are compared in Table 3. The results predict that the system thrust ratio for configurations 4 is fairly accurate with an increase of 0.51%. The system thrust ratio for configuration 5, with a 90° injection was predicted with a 3.1% decrease from PAB3D results. The thrust-vectoring angle was also calculated for this case, but the results indicated a 48.6% decrease. The computations for configuration 4 were achieved using a constant pressure and temperature inlet. However, the results for configuration 5 were achieved using a mass flow inlet with a constant ambient temperature for the secondary injection, in addition to the same boundary conditions used for the primary jet. As discussed in previous sections, the correct inlet boundary conditions for the primary nozzle and secondary nozzle are constant temperature and pressure. Therefore, configuration 4 was set with correct boundary conditions, which explains the accurate predictions. Configuration 5 was not set with the correct boundary conditions in this case. Thus, ANYS Fluent results shown in Table 3 are inaccurate for configuration 5. The correct solution can also be acquired using the mass flow inlet boundary condition, but the temperature needs to be predicted correctly. From the results, it can be concluded that configuration 5 was inaccurate due to the ambient temperature for the secondary injection and needs to be calculated with the proper boundary conditions. The primary objective for this section was to compute preliminary result for an injected nozzle and to observe if fluent could provide a converged solution for this case. The future studies, in the next sections do not concentrate on short nozzle; therefore no further investigations were completed for this section.

A grid Generation study was completed for this case and the results of this study are presented in Table 4. The initial grid generated was very fine for this study, thus the amount of cells were reduced by over half of the total cells. The results from this study provided a 0.0%

difference in the calculated system thrust ratio, which conform the correct grid density used for mesh generation.

Configuration	Computational Code	Injection Angle	$C_{f,sys}$	δ (TV Angle)	% Difference, $C_{f,sys}$
4	PAB3D	0	0.976	0	0.51
4	ANSYS Fluent	0	0.981	0	
5	PAB3D	90	0.965	5.7	3.1
5	ANSYS Fluent	90	0.935	11.1	

Table 3: Comparison of computational results with PAB3D for configurations 4 and 5

	Number of grid Cells	$C_{f,sys}$
Initial	420,000	0.981
Reduced	160,000	0.981
% Difference	61.9%	0%

Table 4: Results from Grid Generation Study.

C. 2D Nozzle

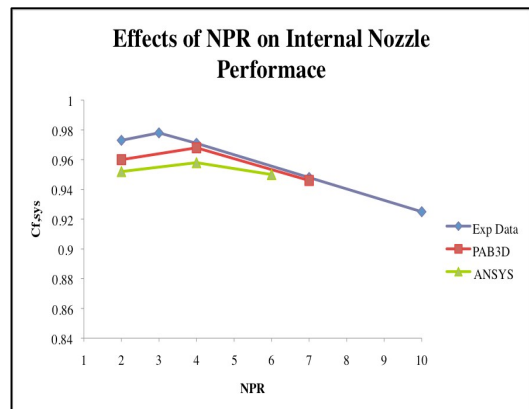
ANSYS Fluent was used to investigate the effects of a tertiary injection on a two dimensional nozzles. Previous experimental and computational works at NASA Langley have confirmed that the current geometry, with cavity length of 3, can achieve greater thrust vectoring angles and internal performance^{1,11}. This paper further investigates the nozzle performance of the

2D geometry by adding a tertiary injection at the downstream throat. Computational results from reference 2 provide thrust vectoring efficiencies of up to 2.15°/% injection, with no aft deck, for 2D geometries with cavity length of 1. The DTN nozzle, with cavity length of 3, provides efficiencies of up to 5°/% injection. Therefore, this geometry was selected for investigation of tertiary injections.

The Experimental data from previous section are used to compare to the computational solutions from ANSYS Fluent and the tertiary injection was added to improve the thrust vectoring efficiency of the current DTN nozzle. All experimental results were achieved with a freestream static pressure and a freestream Mach number of 0.01 for computational stability. The current study predicts nozzle performance and thrust vectoring efficiencies for configurations 6 – 13 with pressure ratios from 3 to 8. A 2.8% injection was used for all secondary and tertiary injections ports.

1. Experimental and Computational Comparison

Computational results for configuration 6 and 7 were achieved for comparison to experimental results and to use for a baseline of the study. The results from configuration 6 with no secondary injection are shown in Figure 27. This figure predicts that the results from ANSYS Fluent are fairly accurate as compared to the experimental and PAB3D. As NPR decreases, the results from ANSYS Fluent and PAB3D do become less accurate. This is due to do the nozzle becoming over expanded.



(a) System thrust ratio

Even though both codes can provide accurate information for under expanded flow, they will always have some inaccuracies for over expanded cases. The codes use experimental data to calculate the results for k-epsilon models. This can provide very accurate results for under expanded flow, but it will start to have inaccuracies as the flow becomes over expanded. Therefore, the study will focus on NPRs of 3 to 8 from this point on. The system thrust

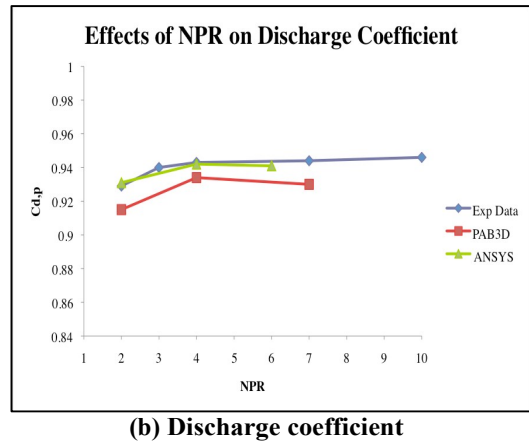
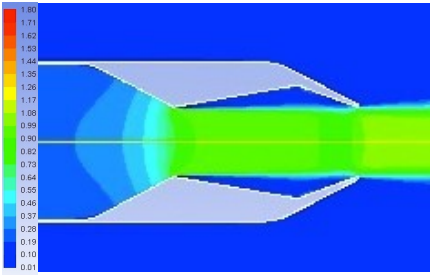


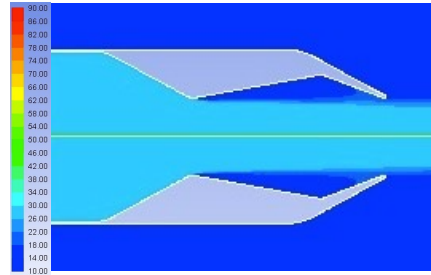
Figure 27: Comparison of experimental and computational nozzle performance, configuration 6. No injection.

ratio picks at NPR of 3 for this case. This is caused by the DTN nozzle as mentioned in previous sections. The system thrust ratio of a typical convergent nozzle peaks at its NPR_D . The NPR_D of this configuration is 2, but the upper and lower cavities separate the flow and change the nozzle performance for lower NPRs. Even though there is no secondary injection in this case, the nozzle cavities are still present and do affect the flow. The thrust ratio is then decreased as the flow becomes highly under expands. This can be shown from the Mach, total pressure, and total temperature contours in Figure 28, Figure 29, and Figure 30. As the total temperature and the total pressure input for the primary nozzle increase, the expansion fans at the exit of the nozzle become stronger. The total pressure also decreases within the cavities at higher values as the NPR increases. Thus, as the flow becomes under expanded, the total pressure loss decreases.

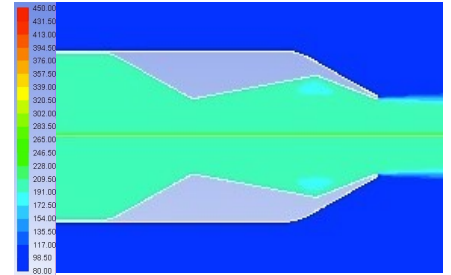
The Discharge ratios for the current configurations are very similar to experimental plots. The discharge ratio is predicted to decrease at lower NPRs. This is simply the mass flow rate of the primary nozzle to the ideal mass flow rate. As the NPR decreases, the effects of the cavity lower the performance of the mass flow rate, thus decreasing the discharge coefficient. It is important to note that ANSYS Fluent does not provide more accurate results since most



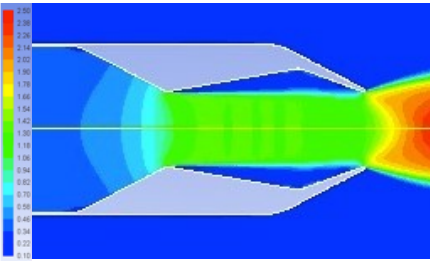
(a) NPR 2



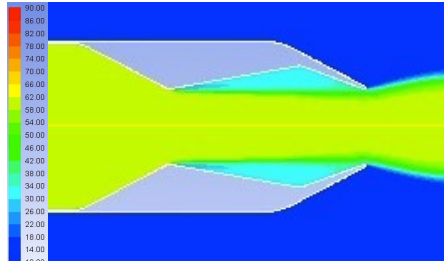
(a) NPR 2



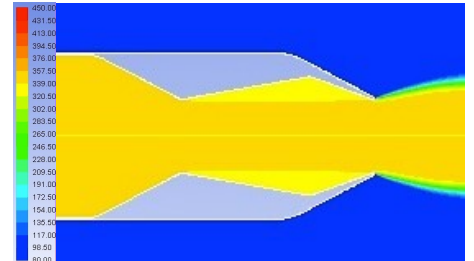
(a) NPR 2



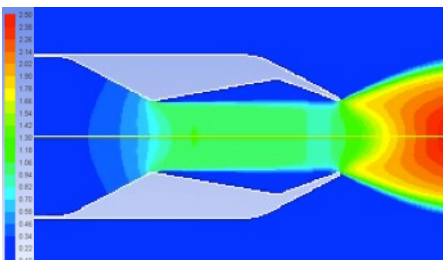
(a) NPR 4



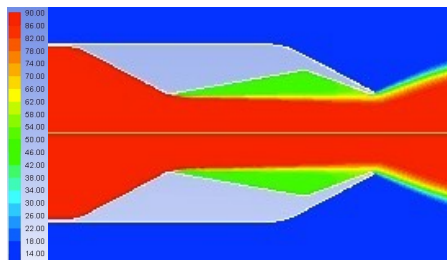
(a) NPR 4



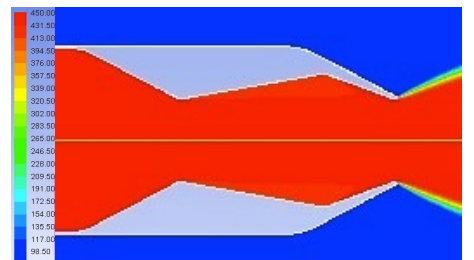
(a) NPR 4



(a) NPR 6



(a) NPR 6



(a) NPR 6

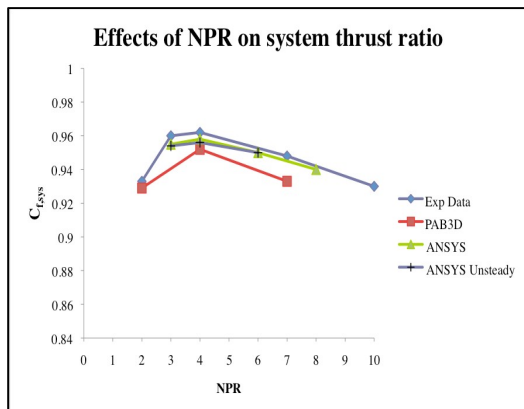
Figure 28: Mach contours for Configuration 6, no injection

Figure 29: Total pressure contours for configuration 6, no injection

Figure 30: Total temperature contours for Configuration 6, no injection

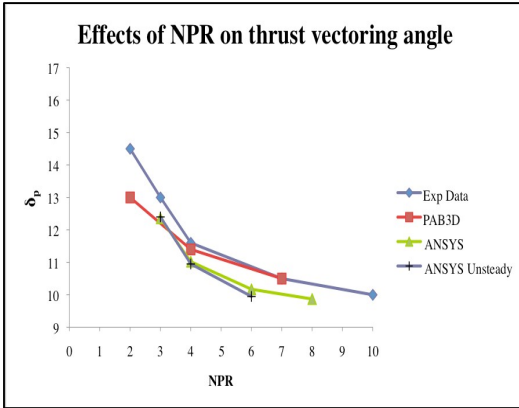
computations from this study match experimental data much closer than PAB3D. The results from the experimental nozzle were achieved with viscous sidewalls for this 2 dimensional nozzle, which included a width of 4 inches. The computational results from PAB3D and ANSYS Fluent neglect the effects of these walls due to the 2D grid used. The experimental design also uses a row of injections holes instead of a slit. Therefore, the results from the CFD are expected to be different than the experimental and if one code provides closer results, it does not conform the accuracy of the code compared to the other. The CFD results are to be used for guidance of the nozzle design and predict which design should be experimentally tested. Another difference between the results from this paper and the experimental is the 3% injection. The experimental results use 3.03% injections, but a 2.8% is used for this study. This does not change the internal performance compared to experimental results much, but it does effects the wall pressures and the thrust vectoring angles, which will be discussed later in this section.

The results from Mach, total pressure, and total temperature contours shown in Figure 28 through Figure 30 were expected prior to CFD calculations. The flow is fully detached within the cavity and this can be shown from the Mach contours. The total pressure loss inside the cavities can provide reasoning to why the system thrust ratio and the discharge ratio are lower than



(a) System thrust ratio

typical convergent nozzles. The total temperature can show this as well, but it is less complicated to see this from the pressure contour. The total pressure and total temperature contours follow each other very closely. This might be difficult to see due to the range of the contours, but the total temperature and total pressure do affect each other. It is also important to note that for



(b) Thrust vectoring angle

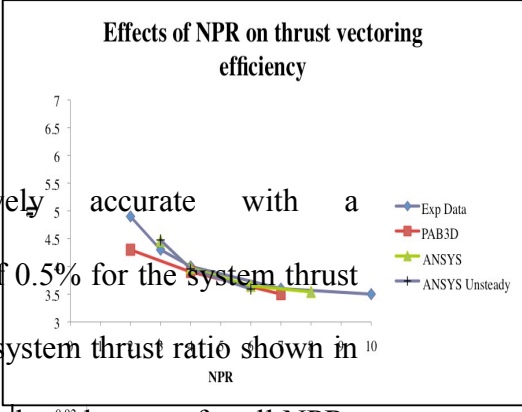
DTN nozzles with area ratios of 1, the sonic line is located at the second throat due to the full separation of the flow from the cavity. This is however, not true area ratios greater than 1.

The results from configuration 7 were also

Figure 31: Comparison of experimental and computational nozzle performance, configuration 7, 2.8% injection.

(c) Thrust vectoring efficiency

(d) Discharge ratio



comparatively

accurate with a

decrease of 0.5% for the system thrust

ratio. The system thrust ratio shown in

Figure 31a does decrease for all NPRs

with the fluidic injection compared to

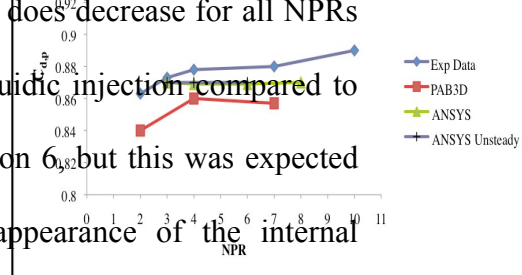
configuration 6, but this was expected

with the appearance of the internal

shocks between the upstream and the

downstream throat shown in Figure

34a through Figure 34d. The



results for system thrust ratio were also predicted to

be lower than experimental due to the 2.8%

injection. The flow experiences more separation

than it would with a 3% injection and this would

have a negative impact on the performance of this

nozzle. The system thrust ratio also peaks at NPR of

4 instead of NPR of 3. This is due to the fluidic

injection lowering the exit static pressure. As the

fluidic injection is applied, the NPR_D modifies. An

NPR_D of 2 is no longer valid and the flow becomes

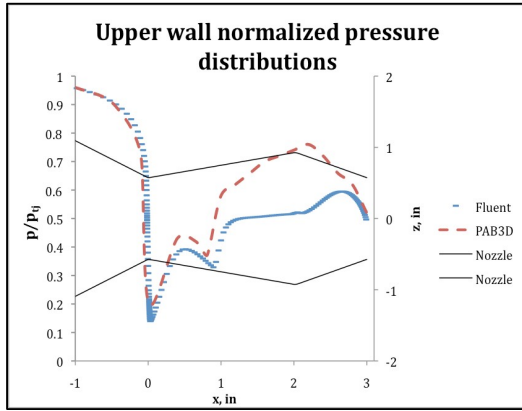
over expanded at this NPR. The thrust vectoring angles and the thrust efficiencies for

configurations 7 are demonstrated in Figure 31b and Figure 31c. The results for thrust vectoring

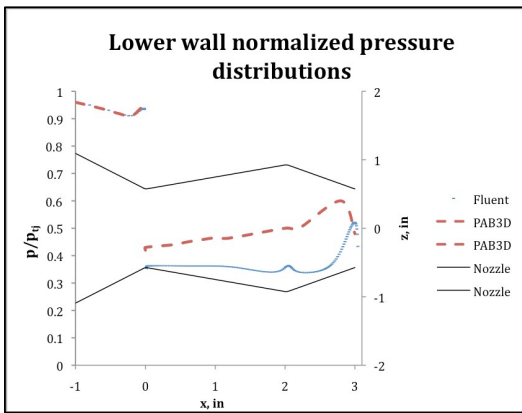
angles were predicted to be lower than experimental due to the secondary injection of 2.8% instead of 3%. The results from thrust vectoring efficiencies were accurate within 3.7%. The thrust vectoring efficiency is the ratio of thrust vectoring angle to the percentage of injection. This predicts that ANSYS Fluent's results can achieve thrust-vectoring angles similar to the experimental at a secondary injection of 3%. This also predicts that the results from Figure 31b are accurate. As stated above, the experimental nozzle is equipped with injection holes and includes the viscous sidewalls; therefore the computational results are not to be fully accurate. The discharge ratio for the current configurations is shown in Figure 31d. The discharge ratio predicts a 1% decrease from experimental results for most NPRs. Even with the addition of the secondary injections, the system discharge ratio does provide lower results at lower nozzle pressure ratios due to the effects of the cavity.

Unsteady solutions were also computed and demonstrated for all nozzle performances in Figure 31. The results predicted are less than 1% difference from the steady state solutions. The Mach, static pressure, total pressure, and total temperature also predicted no change. Thus, it is concluded that steady state solution can predict the end results for this unsteady problems.

The experimental and computational normalized upper and lower wall pressures for NPR 4 are shown in Figure 32. Even though the results from the nozzle performance were predicted very accurately, the wall pressures are not close as predicted. All solutions from this paper were acquired using a 2.8% injection. This does not have a large impact on the nozzle performance, but it does affect the upper and the lower wall pressures. The top wall pressures are identical for experimental results upstream of the nozzle, but experimental results predicted a longer expansion before the shock post upstream throat. This is due to the higher percentage injections. The flow from experimental results is also less separated ($1.1 < x < 2.8$) since the injection percentage is higher; however, this does affect the bottom wall pressure as well. The Mach



(a) Upper wall pressure



(b) Lower wall pressure

Figure 32: Comparison of PAB3D and Fluent wall pressures for configuration 7, NPR=4, 2.8% injection.

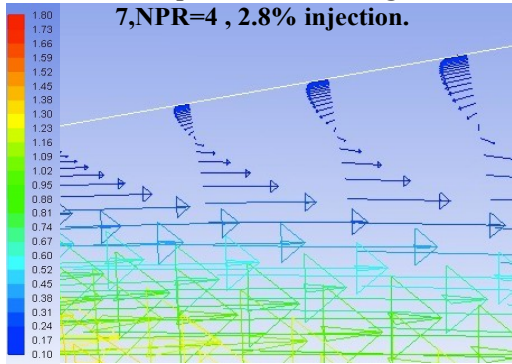
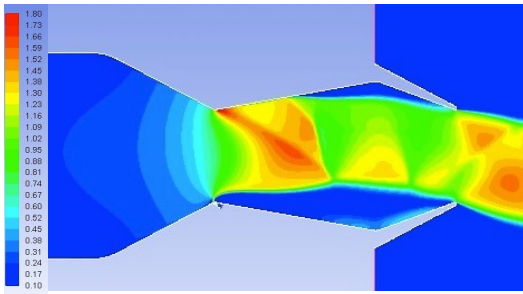


Figure 33: Velocity vectors at $x = 1.1$ inch. Configuration 7, NPR4, 2.8% injection.

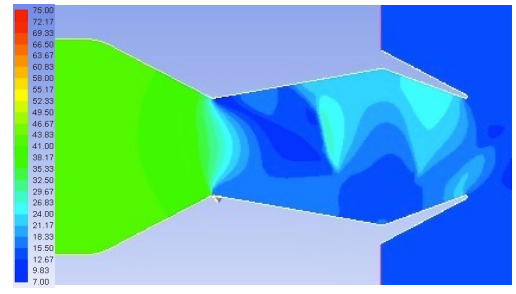
contours in Figure 34 can demonstrate where the flow is separating from the top wall. The DTN nozzle achieves its high thrust vectoring performance from the pressure differential of the upper and lower wall and Figure 32 shows that even though the upper wall pressure decreases, the lower wall pressure also decreases. This can explain why the same thrust vectoring efficiencies can be acquired from these configurations. Therefore, it can be concluded that the wall pressures differ due to the 0.2% difference of the secondary injection.

Mach, static pressure, total pressure, and total temperature are demonstrated in Figure 34 through Figure 37. It is shown from the Mach contours that the structure of the flow does not change much as the NPR increases, but the flow becomes highly under expanded. The static pressure contours show that as the NPR increases, the shocks downstream of the first throat become stronger. The Mach contour can also demonstrate the shocks within the flow, but this can be seen much more clearly from the pressure differential upstream and downstream of the shocks in Figure 35.

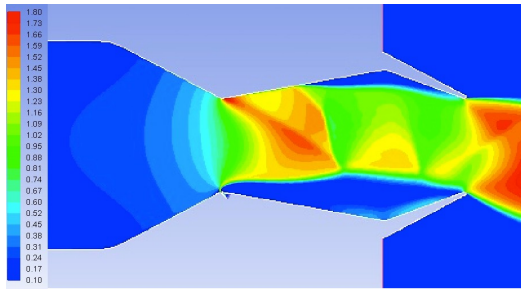
The flow is detached at about $x = 1.1$ inch from the first throat. This can be shown from the velocity vectors from Figure 33. As the flow detaches from the wall, a reverse circular flow is



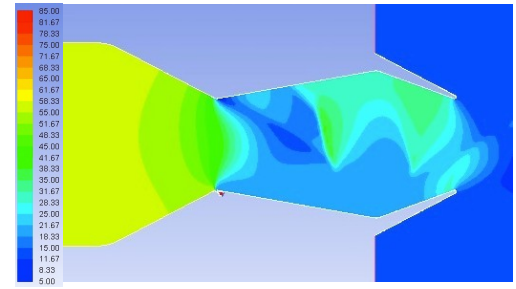
(a) NPR 3



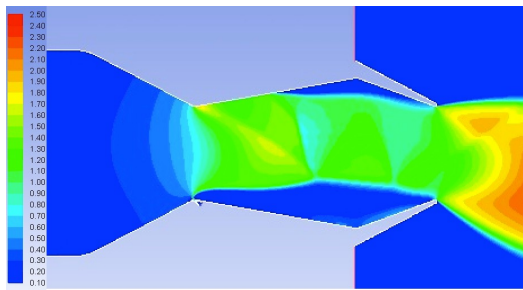
(a) NPR 3



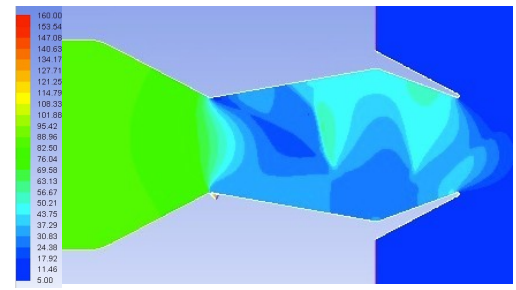
(b) NPR 4



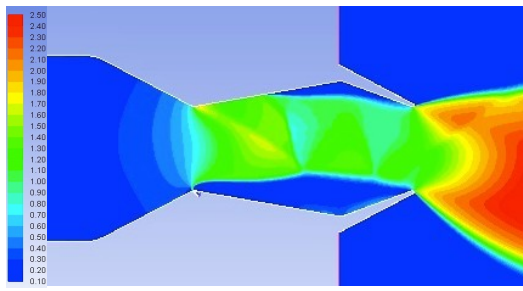
(b) NPR 4



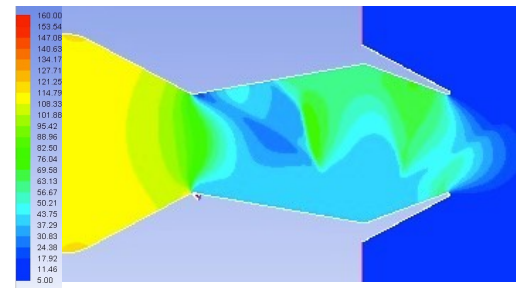
(c) NPR 6



(c) NPR 6



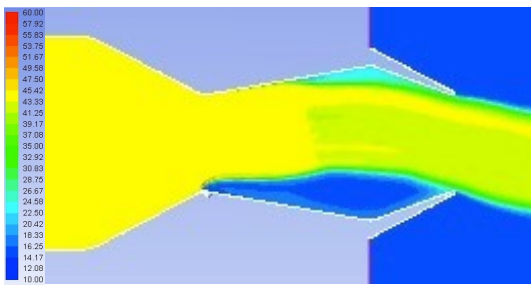
(d) NPR 8



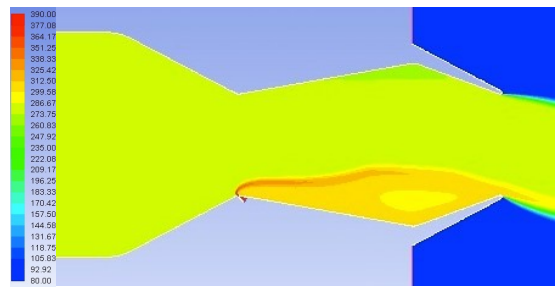
(d) NPR 8

Figure 34: Mach contours for configuration 7, 2.8% injection

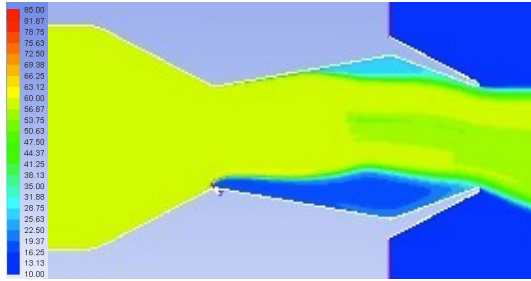
Figure 35: Static pressure contours for configuration 7, 2.8% injection



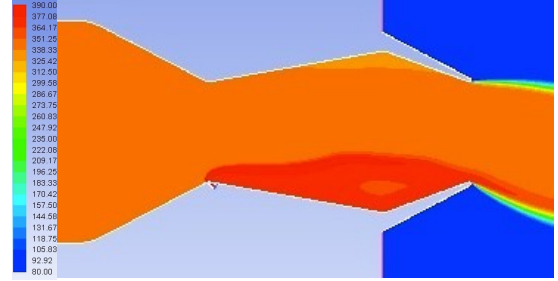
(a) NPR 3



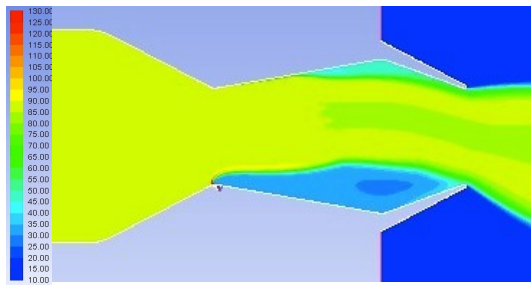
(a) NPR 3



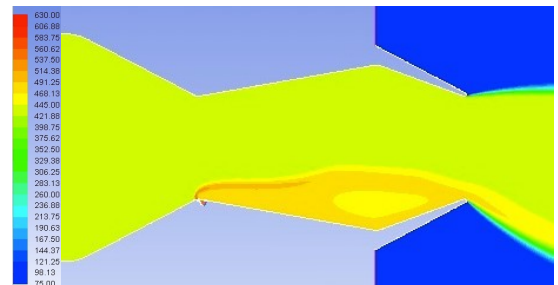
(b) NPR 4



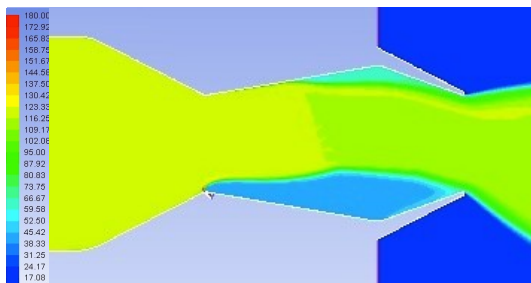
(b) NPR 4



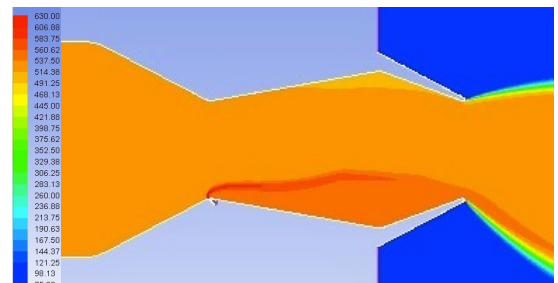
(c) NPR 6



(c) NPR 6



(d) NPR 8



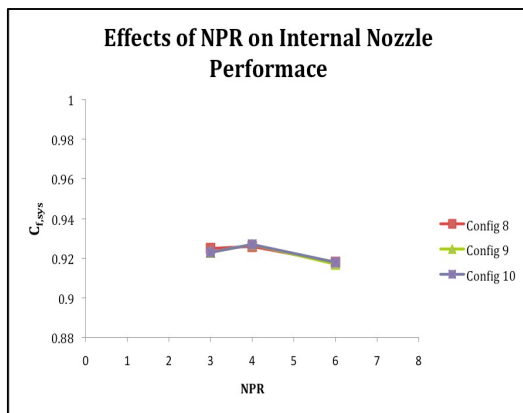
(d) NPR 8

Figure 36: Total pressure contours for configuration 7, 2.8% injection

Figure 37: Total temperature contours for configuration 7, 2.8% injection

developed on the upper wall. This is much like the detached flow from the bottom wall, but this region is extremely smaller. The total pressure and total temperature can demonstrate the irreversibility of the flow past the shock. As the flow travels through the shock, the total pressure and the total temperature decrease and they cannot recover due to the irreversibility of the flow. Figure 36 can demonstrate the pressure losses through the shock and the near by the upper and lower walls. When compared to Figure 31a, it can be shown that as the total pressure loss decreases, the system thrust ratio also decreases. The total temperature also decreases, as the total pressure decreases after the shock. This is not shown in Figure 37 due to the contour range, but the viscous losses at the upper and lower walls can be visualized.

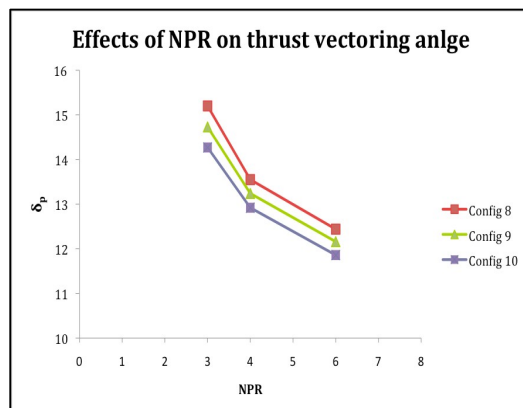
2. Effects of external tertiary injection



(a) System thrust ratio

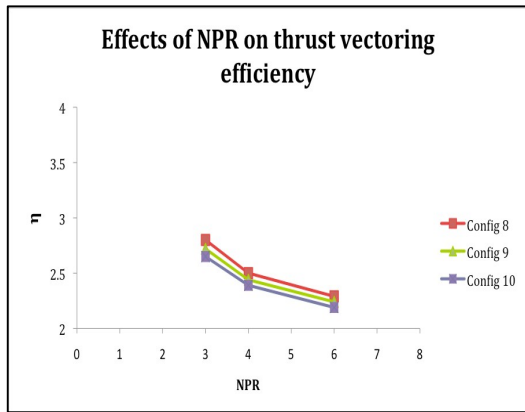
The predictions for configurations 8, 9, and 10 for the system thrust ratio, thrust vectoring angle, thrust vectoring efficiency, and system discharge coefficient are shown in Figure 38. The system thrust ratios for all cases are very similar, but there is a

(b) Thrust vectoring angle

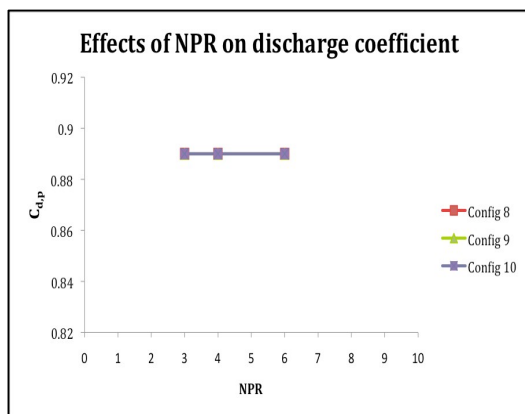


3.6% decreases from configuration 7. This is due to the tertiary injection, which adds a third variable to

equation 5. Since the ideal isentropic thrust of the tertiary injection is added to the denominator in equation 5, the system thrust ratio for all nozzles with tertiary injections decreases. It is predicted that configuration 8 provides a very small increase in the



(c) Thrust vectoring efficiency



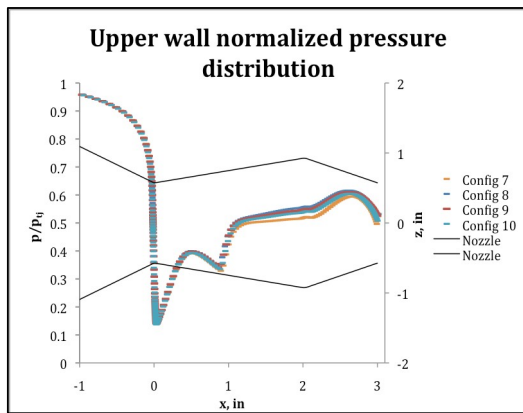
(d) Discharge ratio

Figure 38: Computational nozzle performance for configuration 8,9,and 10. 2.8% injection.

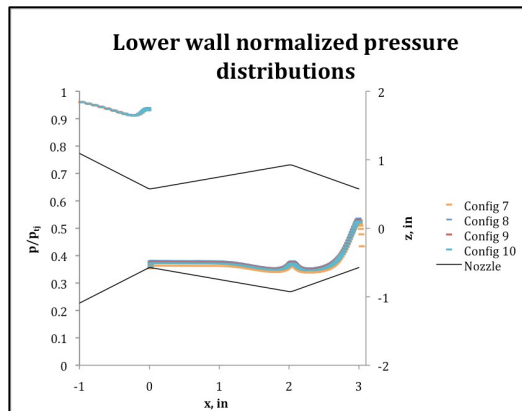
system thrust ratio at NPR of 3 and a small decrease at NPR of 4 when compared to configurations 9 and 10. The external injection is located outside of the nozzle and it is to further redirect the primary flow after separation from the nozzle. Thus, as the flow becomes highly under expanded and closer to the injection, the tertiary injections will impact the plume more. This does not affect the total pressure for configurations 9 and 10, but it effects configuration 8 due to the high injection angle. Therefore, the higher angle will affect the total pressure loss at NPRs of 3 and 4. This does not occur at NPR of 6 since the flow is highly under expanded. As stated, the injections affect the total pressure loss inside the nozzle as NPR varies. This can be demonstrated from the total

pressure loss shown in Figure 42. As the NPR increase, the total pressure loss increases. However, when compared to configuration 7, less total pressure is lost. The external injection is to further redirect the flow to achieve higher thrust vectoring angles, but this adds the tertiary injection to equation 5 and reduces the system thrust ratio. Thus, Even though less total pressure is lost for this case, the system thrust ratio will still decrease. On the other hand, the external injection increases the thrust vectoring angles up to 16%. Figure 38b predicts higher thrust vectoring angles as the angle of the injection increases. The thrust vectoring efficiency does decrease from configuration 8 - 9, but this should not be compared to configurations with no

tertiary injections. The thrust efficiency is the ratio of thrust vectoring angle to the percentage injection. Since the percentage injection is nearly doubled with the tertiary injection, it is expected for the thrust efficiency to dramatically decrease. The discharge ratios for the external tertiary injections shown in Figure 38d are also very similar. The discharge ratios are higher than configuration 7 and this is simply due to the addition of tertiary injection.



(a) Upper wall pressure

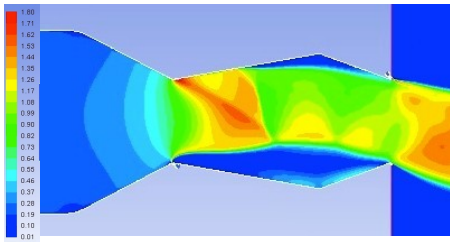


(b) Lower wall pressure

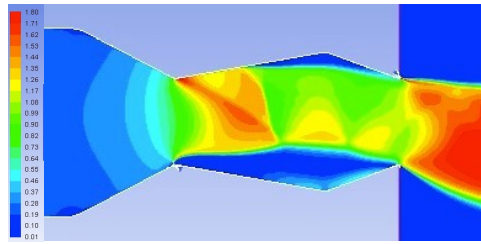
Figure 39: wall pressures for configuration 7-10, NPR=4 , 2.8% injection.

The wall pressures for configurations 8, 9 and 10 at NPR of 4 are shown in figure 31. The upper and lower wall pressures are similar when compared to configuration 7. The upper wall pressures for configuration 7, shown in orange, are lower than the configurations with tertiary external injection. This is due to the external injections creating a higher static pressure region at the upper cavity wall. Since the lower wall pressures do not change as much, a higher pressure differential is created and a higher thrust vectoring angle is achieved. Also as the tertiary thrust vectoring angle increases, higher pressures are acquired on the upper wall. This results to less separation at the upper wall and slightly higher thrust vectoring angles shown in Figure 38b.

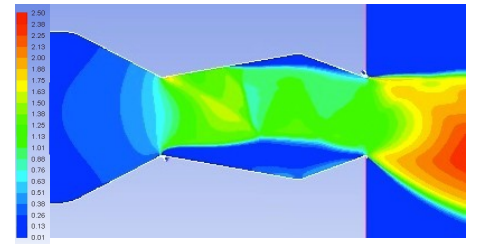
The Mach, Total pressure, static pressure, and total temperature for configurations 8, 9, and 10 are shown in Figure 40 through Figure 43. The flow is similar to the configuration 7 and the effects of the tertiary injection can be observed from the Mach contours at exit conditions. As the injection angle increases, the increase in thrust



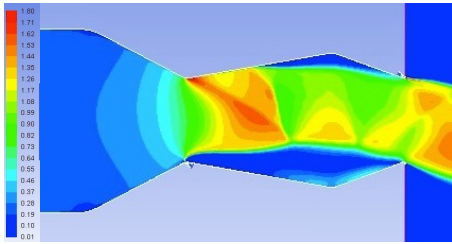
(a) Configuration 8, NPR 3



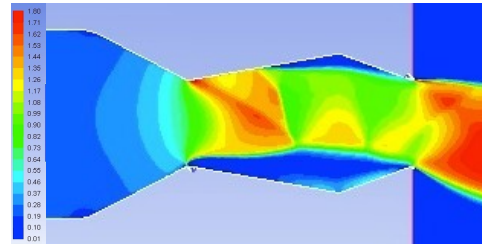
(b) Configuration 8, NPR 4



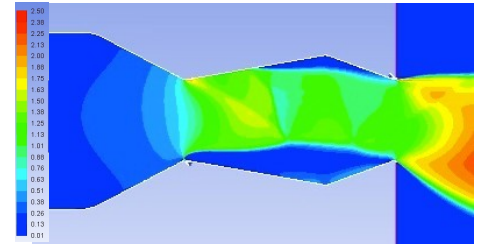
(c) Configuration 8, NPR 6



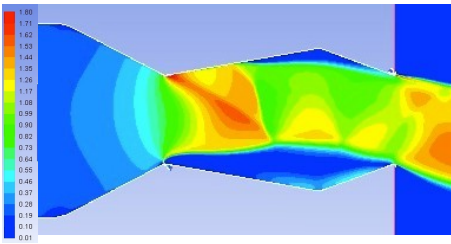
(d) Configuration 9, NPR 3



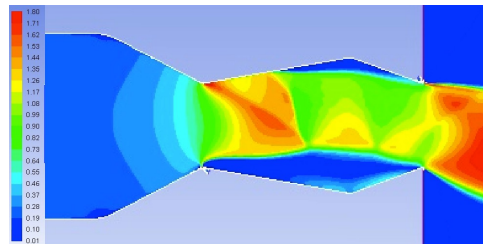
(e) Configuration 9, NPR 4



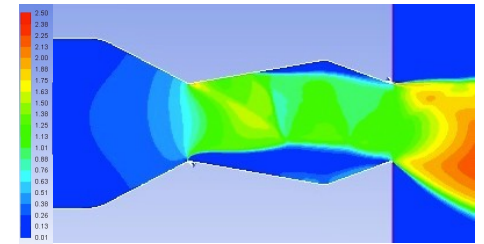
(f) Configuration 9, NPR 6



(g) Configuration 10, NPR 3

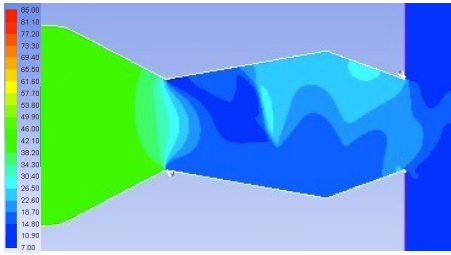


(h) Configuration 10, NPR 4

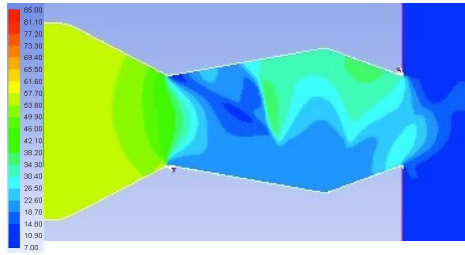


(i) Configuration 10, NPR 6

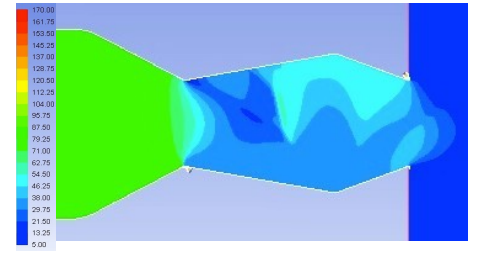
Figure 40: Mach contours for Configuration 8-10, 4% Injection



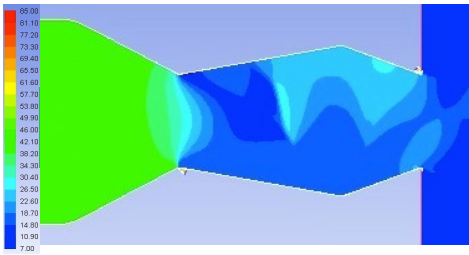
(a) Configuration 8, NPR 3



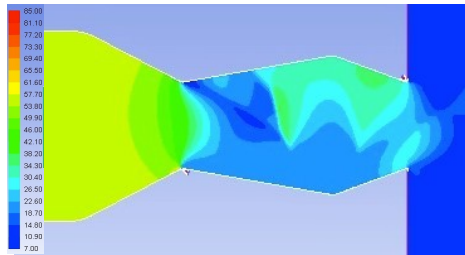
(b) Configuration 8, NPR 4



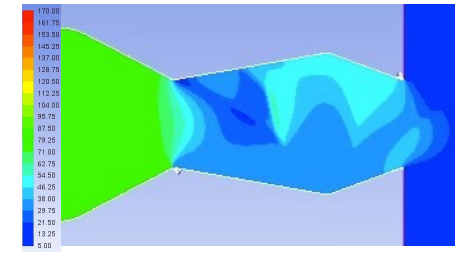
(c) Configuration 8, NPR 6



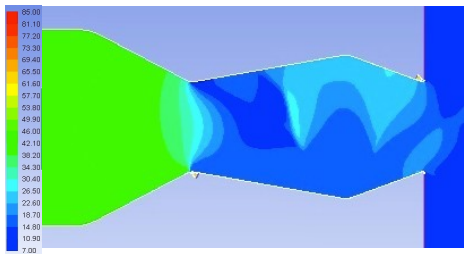
(d) Configuration 9, NPR 3



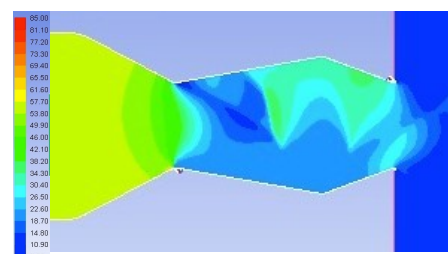
(e) Configuration 9, NPR 4



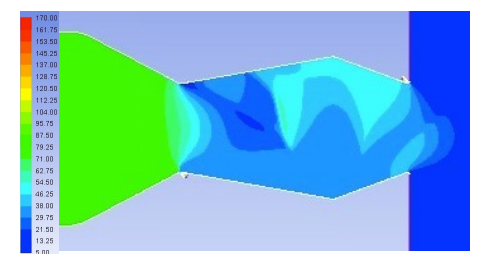
(f) Configuration 9, NPR 6



(g) Configuration 10, NPR 3

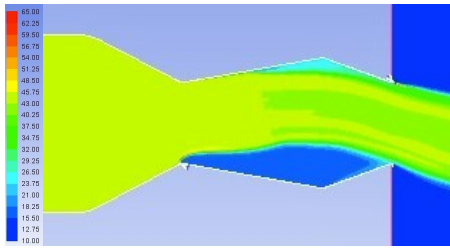


(h) Configuration 10, NPR 4

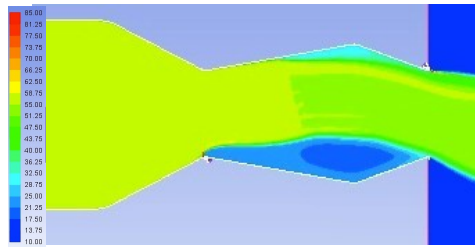


(i) Configuration 10, NPR 6

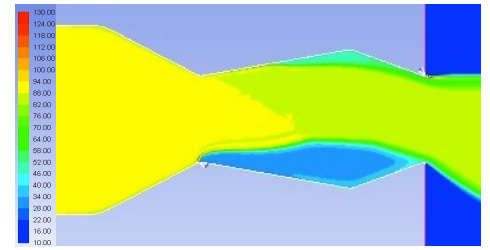
Figure 41: Static contours for Configuration 8-10, 4% Injection



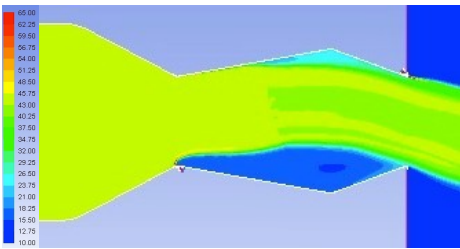
(a) Configuration 8, NPR 3



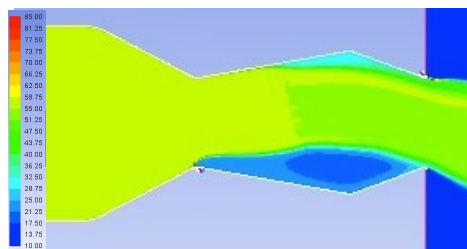
(b) Configuration 8, NPR 4



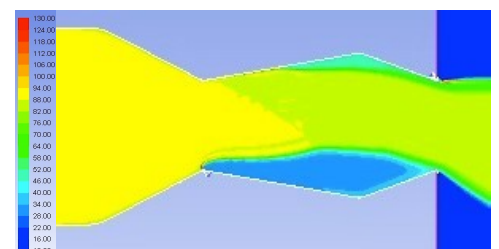
(c) Configuration 8, NPR 6



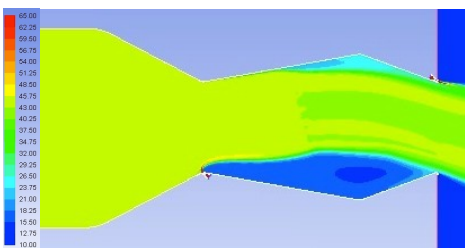
(d) Configuration 9, NPR 3



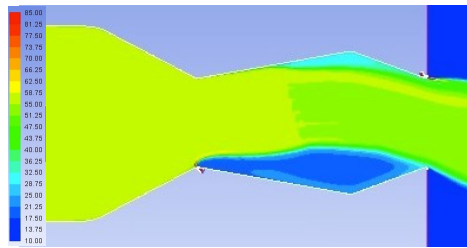
(e) Configuration 9, NPR 4



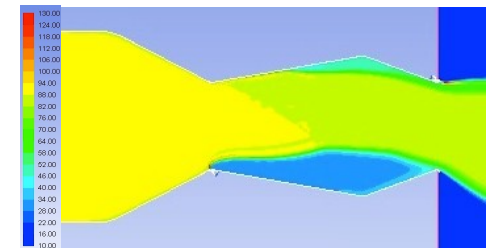
(f) Configuration 9, NPR 6



(g) Configuration 10, NPR 3

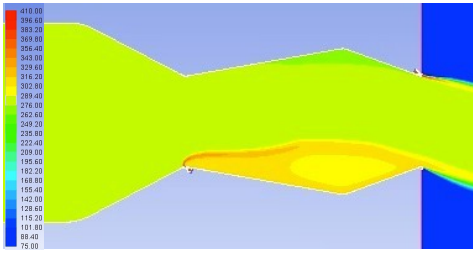


(h) Configuration 10, NPR 4

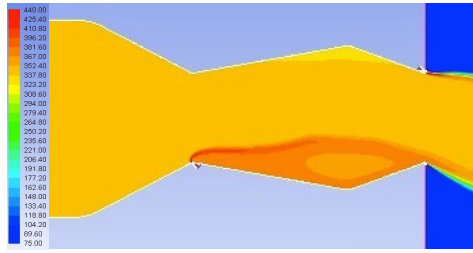


(i) Configuration 10, NPR 6

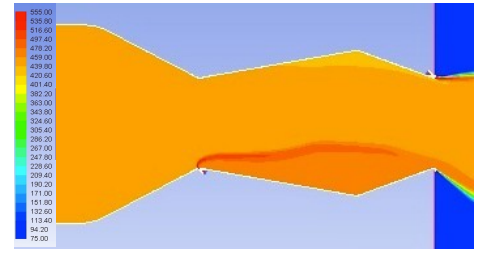
Figure 42: Total pressure contours for Configuration 8-10, 4% Injection



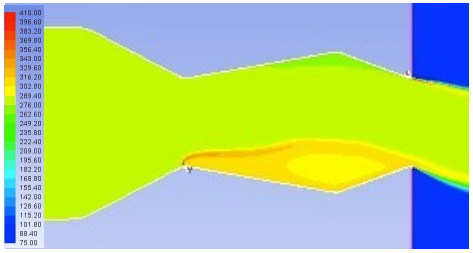
(a) Configuration 8, NPR 3



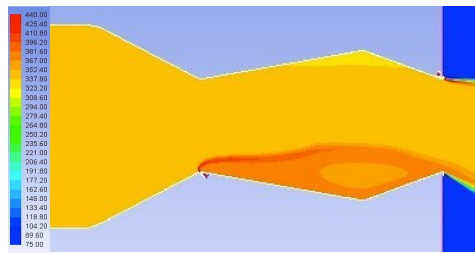
(b) Configuration 8, NPR 4



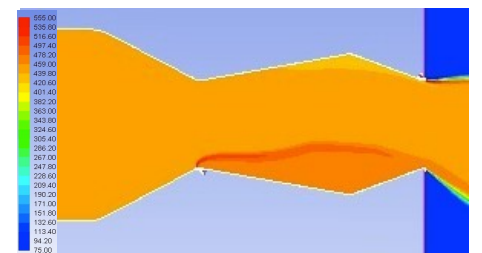
(c) Configuration 8, NPR 6



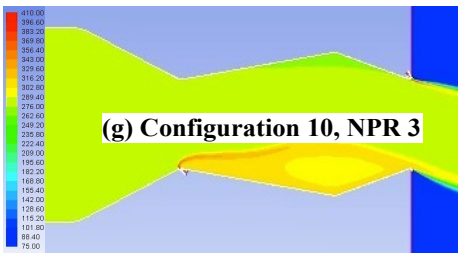
(d) Configuration 9, NPR 3



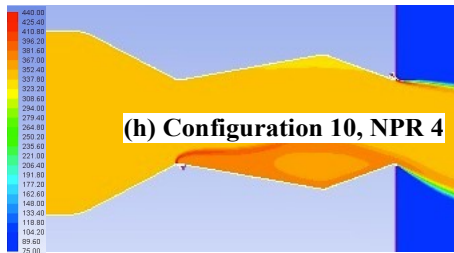
(e) Configuration 9, NPR 4



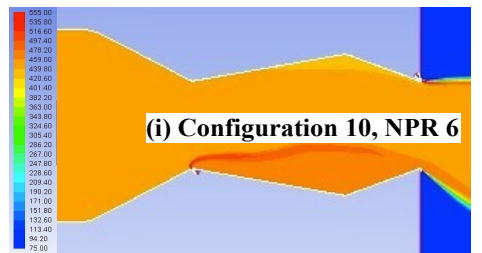
(f) Configuration 9, NPR 6



(g) Configuration 10, NPR 3



(h) Configuration 10, NPR 4



(i) Configuration 10, NPR 6

Figure 43: Total temperature contours for Configuration 8-10, 4% Injection

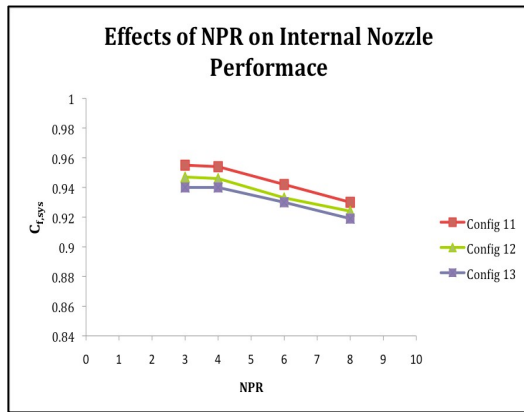
vectoring angle can be observed. The flow experiences the same shocks as configuration 7. The shocks travel through the flow as shown in Mach and static pressure contours (Figure 40 and Figure 41). The flow is still detached from the upper wall as previously discussed, which provides circulation at the upper wall cavity. The total pressure and temperatures demonstrates the pressure losses at the upper wall due to the external injections. It is shown that the total pressure and temperatures do not differ for different configuration at NPRs 3, 4 and 6. This can explain why the system thrust ratio and the discharge coefficients provide the same values for different configurations at different NPRs. The total pressure contours also show that as the flow travels through the shock, it will experience losses in total pressure due to the irreversibility of the flow, but these losses are almost identical at the same NPR for different configurations.

A grid generation study was concluded for the tertiary external injection. The comparison for configuration 8 at NPR of 4 is shown in Table 5. The results indicate a 0.37% decrease in thrust vectoring angle; however, the system thrust ratio and the system discharge ratio predict a 0.01% and 0% change. This is due to change of thrust in the x and the y direction. A decrease in the y velocity was determined and this reduces the thrust vectoring angle, but it provides very similar results for the system thrust ratio and the discharge coefficient. Therefore, it can be concluded that the results from the grid generation study are accurate and there is no need for increasing the initial grid density.

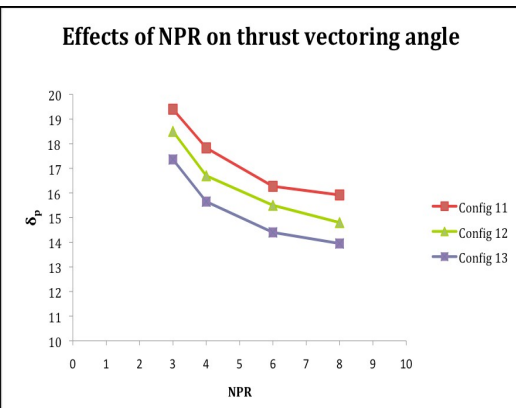
	Number of grid cells	$C_{f,sys}$	$C_{d,p}$	δ_p
Initial	61,000	0.927	0.890	13.54
Increased	125,000	0.927	0.890	13.49
% Difference	52%	0.01%	0%	0.37%

Table 5: Results from Grid generation study. Configuration 8, NPR 4, 2.8% injection

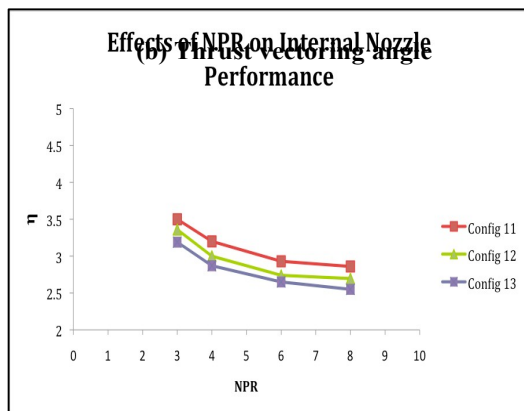
3. Effects of tertiary injection at exit line



(a) System thrust ratio



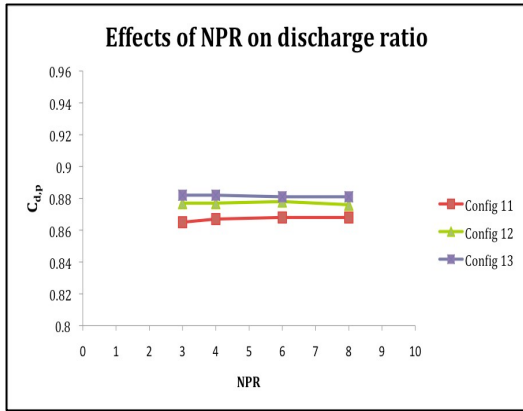
(b) Thrust vectoring angle



(c) Thrust vectoring efficiency

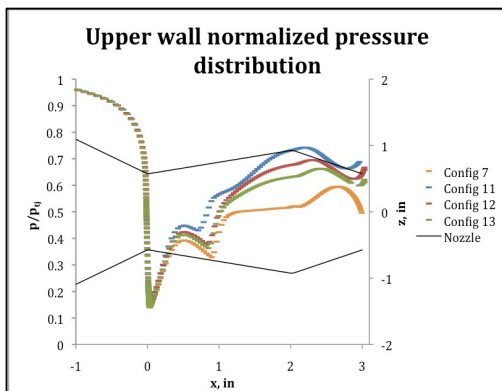
The results for system thrust ratio, thrust vectoring angle, and discharge ratio are provided in Figure 44. The system thrust ratios for all 3 configurations are consistent and do not cross unlike the results from the exterior injections. Figure 44a predicts that as the tertiary injection angle increases, the system thrust ratio increases. The results can be shown from the total pressure and total temperature counters in Figure 52 to Figure 57. As the tertiary injection angle decrease, the band of lower total pressure and temperature against the upper wall thickens and the internal loss from the shock increases. As a result, increasing the tertiary angle will increase the system thrust ratio. However, the consequence of increasing the tertiary injections angle is lowering the discharge coefficient. This can be explained from the decrease of the tertiary injection flow rate entering the exit line and from the decrease of exit mass flow rate due to the tertiary injection.

The injection at the exit of the nozzle creates high-pressure region against the upper cavity wall as shown in Figure 49 to Figure 51. Thus, the flow

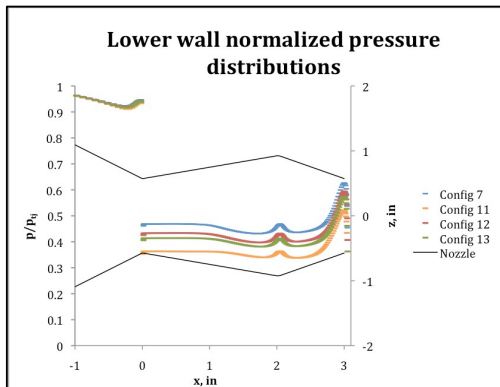


(c) Discharge ratio

Figure 44: Computational nozzle performance for configuration 11, 12, and 13. 2.8% injection.



(a) Upper wall pressure



(b) Lower wall pressure

Figure 45: wall pressures for configuration 10-13, NPR=4, 2.8% injection.

experiences less separation at the upper wall and increases the upper wall pressures as shown in Figure 45a. As the tertiary injection angle increases, this static pressure region at the upper wall cavity increases. Therefore, the upper wall pressures increase at higher injection angles and increase the system

thrust ratio. The Mach contours in Figure 46 through Figure 48 can demonstrate the separation at the upper wall of the cavity. When compared to configuration 7, it can be seen that the flow experiences less separation

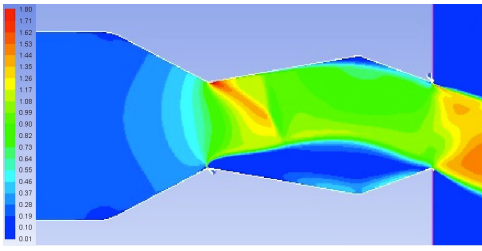
at the upper wall. As the flow separates, a circular reverse flow presents at the upper cavity much similar to Figure 33. This reverse flow region is much smaller than configuration 7; however, this still does slightly impact the system thrust ratio. The Mach and the static

pressure also show shock post upstream throat and the shear layer between the reverse flow at the bottom and the primary flow. The shocks in configurations 7 – 10 travel through the flow, but they do not for exit line tertiary injections. It is shown in Figure 49 that the shocks are stopped at the high-pressure region at the top wall. However, Figure 50 and Figure 51 show that the shocks attempt to move up towards the upper wall,

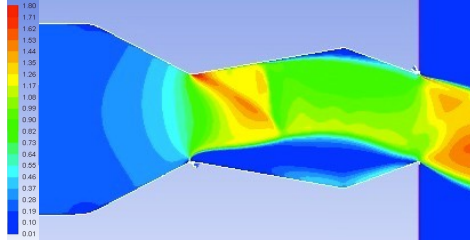
but the high pressure region does not allow this to take place.

Figure 44b - c presents the thrust vectoring predictions. Configuration 11, can achieve up to 51% increase for thrust vectoring angles at NPR of 3 and 46% at NPR of 8. This provides a 6.6° increase for NPR of 3. As predicted, the thrust vectoring efficiency increases with higher tertiary injection angles. As stated previously, this cannot be compared to configuration 7, but there is an average of 22.7% increase from configurations with external injections. Even though configuration 13 is predicted at lower thrust vectoring angles for exit line injections, it still provides an additional 16.9% increase (NPR = 3) to configuration 7.

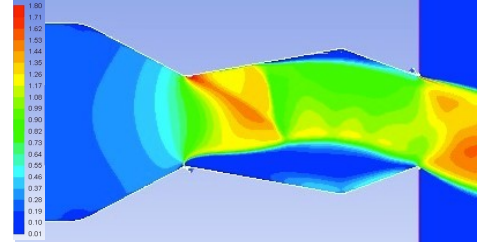
Figure 45 demonstrates the upper and lower wall pressure for configuration 7 and 11-13. Unlike configuration 8-10, the wall pressures for the tertiary injection noticeably vary at different angles. As stated previously, the increase of the tertiary injection angle, increases the upper wall pressures due to the high static pressure built up from the tertiary injection. This also affects the lower wall pressures. As the upper wall pressures increase, the lower wall pressure also increases. This however does not increase the wall pressures evenly. The pressure differential between configuration 7 and configurations 11-13 for upper wall pressures are higher than the pressure differential of the lower walls. Also the tertiary injection further skews the sonic line at the downstream throat due to the sonic flow properties before the second throat. This can be visualized from Figure 46 through Figure 48. This is extremely important since there is no shock from the injection at the downstream throat. Skewing the sonic line at the second throat can provide much higher internal performance efficiencies. If a shock is present at the exit, the system thrust ratio and the discharge would be much lower than what is presented in Figure 44. From this, it can be concluded that it is the combination of this pressure differential and the further skewing of the downstream throat sonic line by the tertiary injection that helps this nozzle achieve such high thrust vectoring angles.



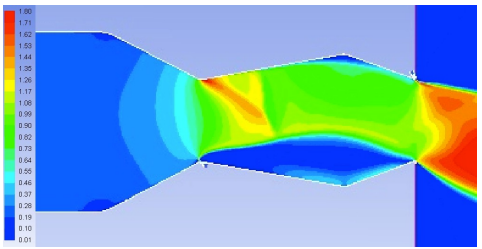
(a) Configuration 11, NPR 3



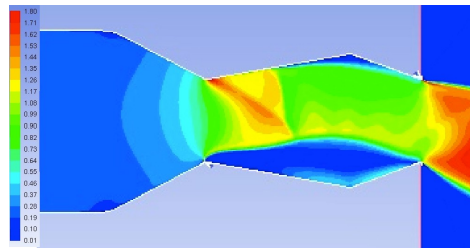
(a) Configuration 12, NPR 3



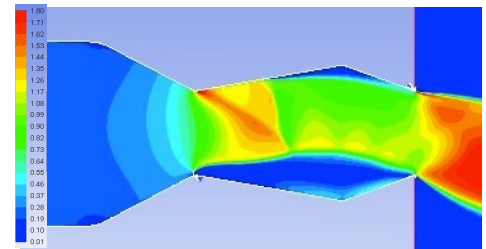
(a) Configuration 13, NPR 3



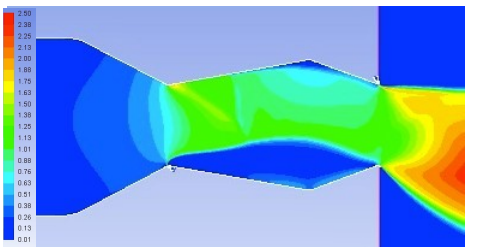
(b) Configuration 11, NPR 4



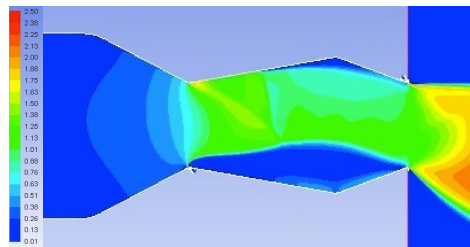
(b) Configuration 12, NPR 4



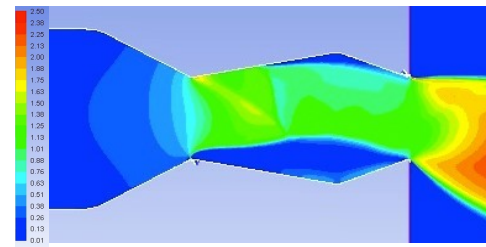
(b) Configuration 13, NPR 4



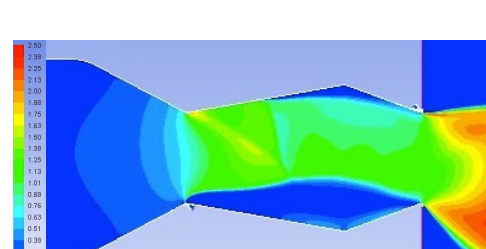
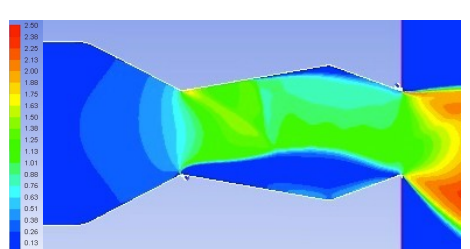
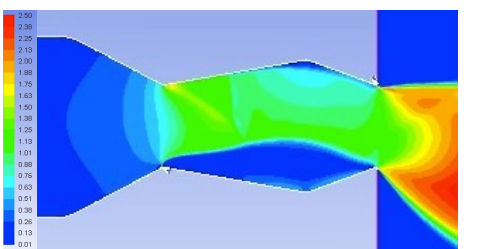
(c) Configuration 11, NPR 6



(c) Configuration 12, NPR 6



(c) Configuration 13, NPR 6



(d) Configuration 11, NPR 8

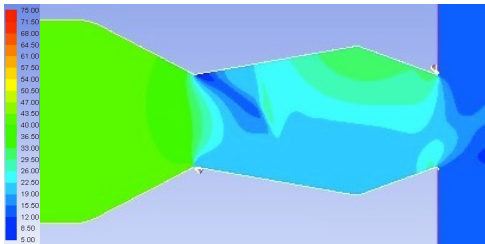
Figure 46: Mach contours for configuration 11

(d) Configuration 12, NPR 8

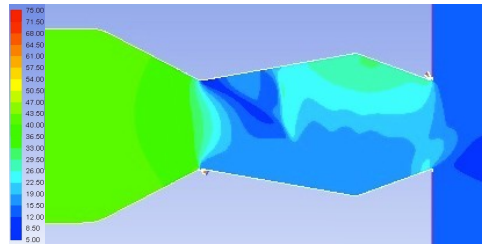
Figure 47: Mach contours for configuration 13, 2.8% injection

(d) Configuration 13, NPR 8

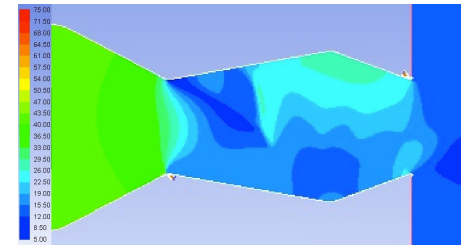
Figure 48: Mach contours for configuration 12, 2.8% injection



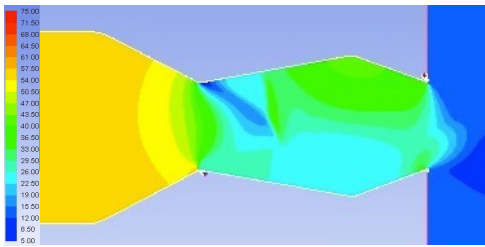
(a) Configuration 11, NPR 3



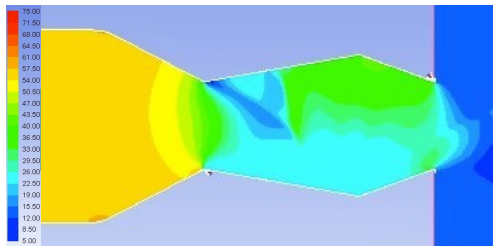
(a) Configuration 12, NPR 3



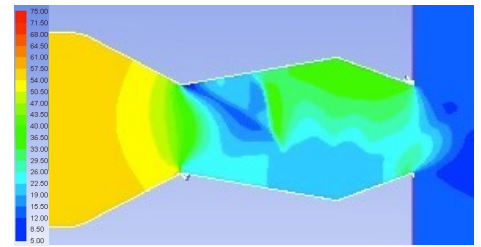
(a) Configuration 13, NPR 3



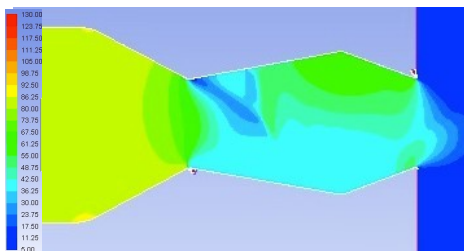
(b) Configuration 11, NPR 4



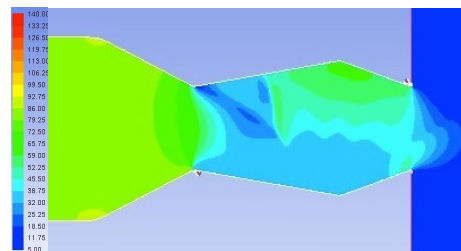
(b) Configuration 12, NPR 4



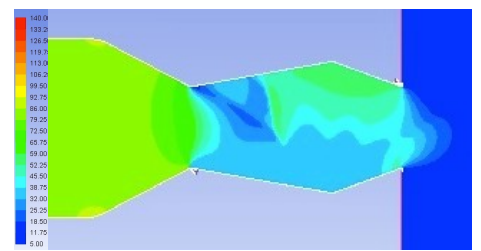
(b) Configuration 13, NPR 4



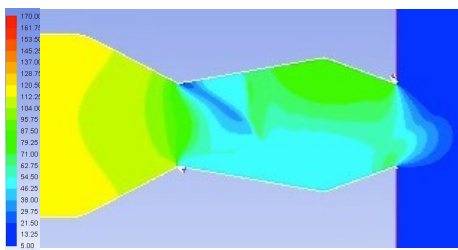
(c) Configuration 11, NPR 6



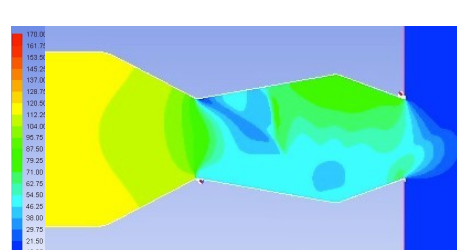
(c) Configuration 12, NPR 6



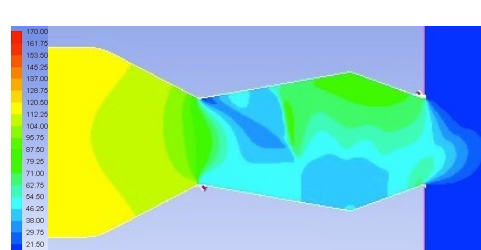
(c) Configuration 13, NPR 6



(d) Configuration 11, NPR 8



(d) Configuration 12, NPR 8

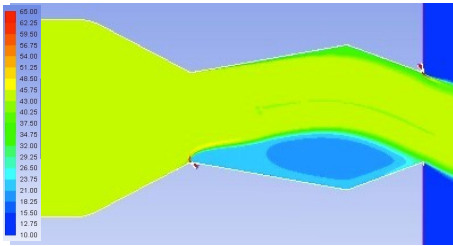


(d) Configuration 13, NPR 8

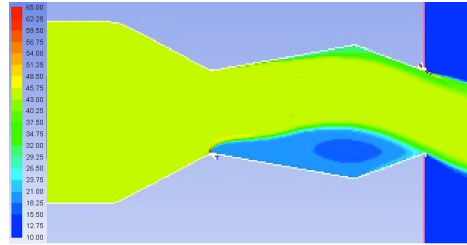
Figure 49: Static pressure contours for configuration 11, 2.8% injection

Figure 50: Static pressure contours for configuration 12, 2.8% injection

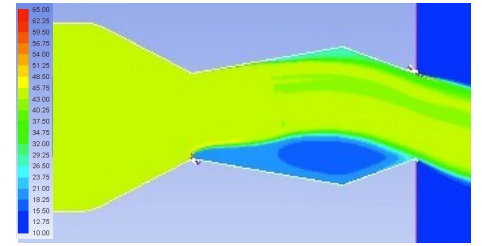
Figure 51: Static pressure contours for configuration 13, 2.8% injection



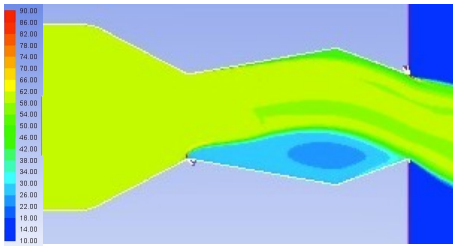
(a) Configuration 11, NPR 3



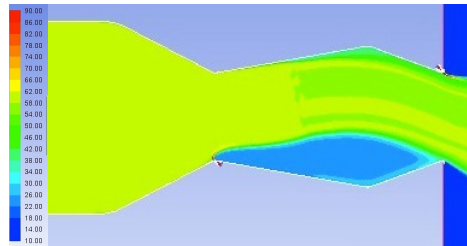
(b) Configuration 12, NPR 3



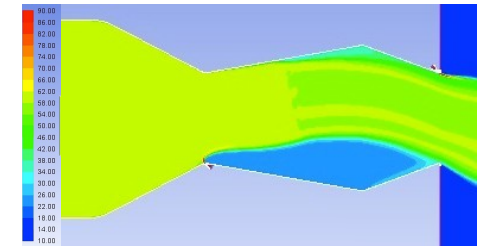
(c) Configuration 13, NPR 3



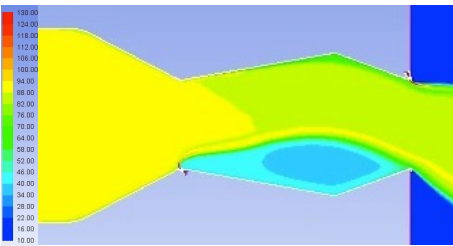
(a) Configuration 11, NPR 4



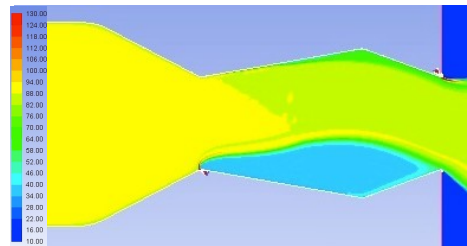
(b) Configuration 12, NPR 4



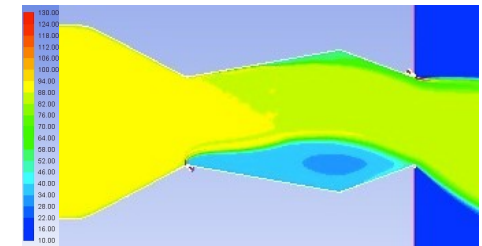
(c) Configuration 13, NPR 4



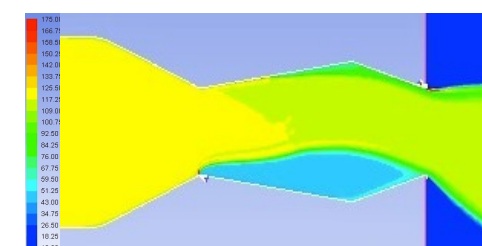
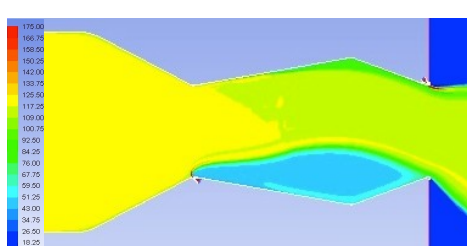
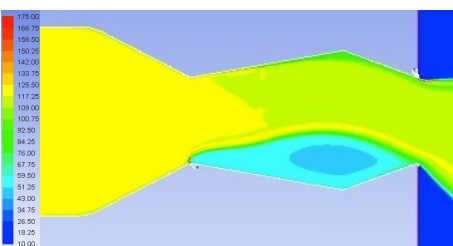
(a) Configuration 11, NPR 6



(b) Configuration 12, NPR 6



(c) Configuration 13, NPR 6



(a) Configuration 11, NPR 8

Figure 52: Total pressure contours for configuration 11, 2.8% injection

(b) Configuration 12, NPR 8

Figure 53: Total pressure contours for configuration 12, 2.8% injection

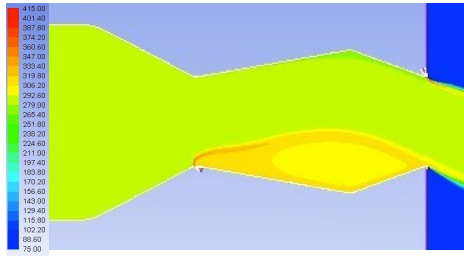
(c) Configuration 13, NPR 8

Figure 54: Total pressure contours for configuration 13, 2.8% injection

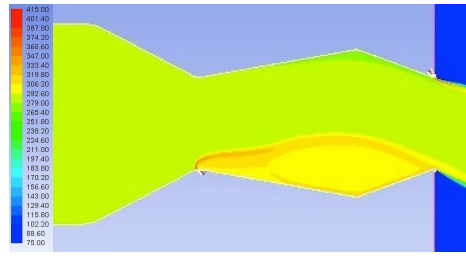
A grid generation study was also completed for configuration 11. The results from this study are provided in Table 6. The results indicate that as the number of grid points nearly double, the percentage difference of the system thrust ratio differs the most when compared to others results. However, this value is only increased by 1%. Thus, it is concluded that the grid density used for all solutions does provide accurate results.

	Number of grid cells	$C_{f,sys}$	$C_{d,p}$	δ_p
Initial	61,000	0.954	0.867	17.83
Increased	125,000	0.955	0.867	17.82
% Difference	52%	1.0%	0.04%	0.05%

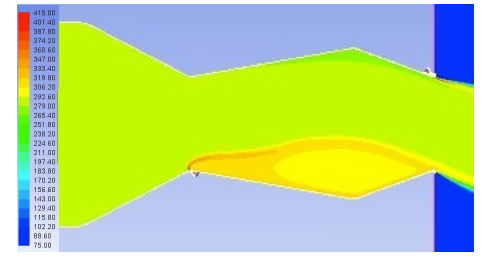
Table 6: Grid generation study results, configuration 11, NPR4, 2.8% injection.



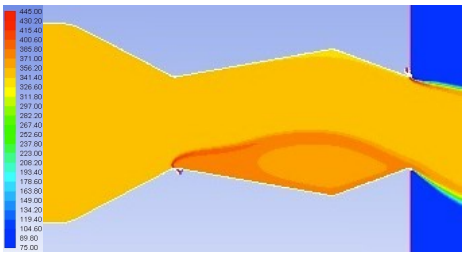
(a) Configuration 11, NPR 3



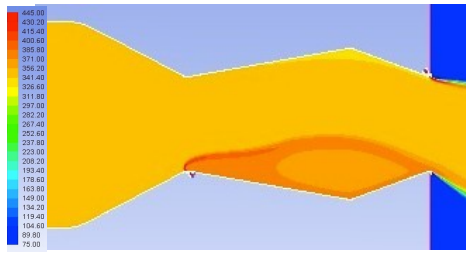
(b) Configuration 12, NPR 3



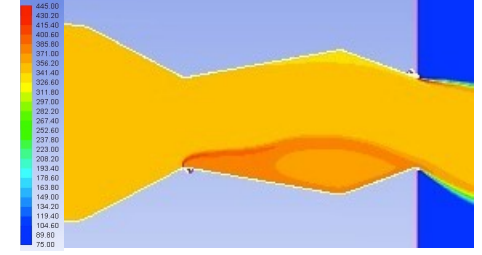
(c) Configuration 13, NPR 3



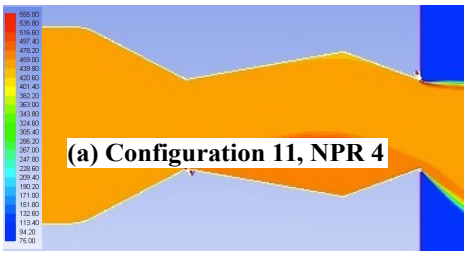
(a) Configuration 11, NPR 4



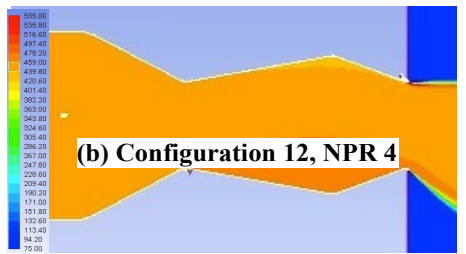
(b) Configuration 12, NPR 4



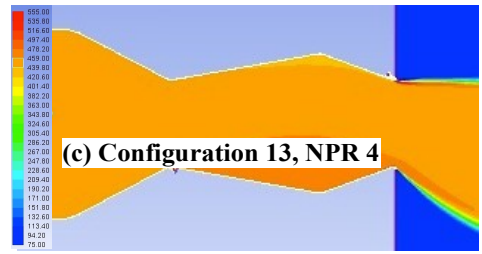
(c) Configuration 13, NPR 4



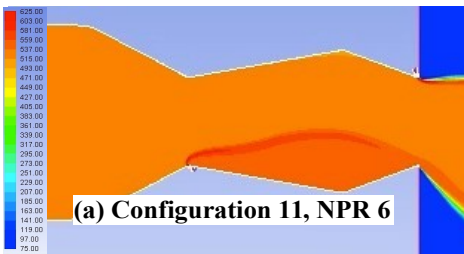
(a) Configuration 11, NPR 6



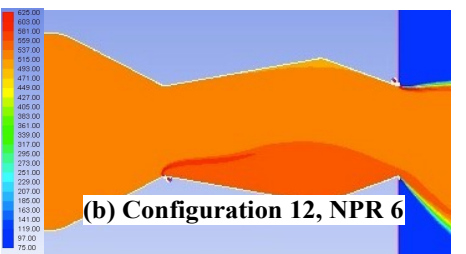
(b) Configuration 12, NPR 6



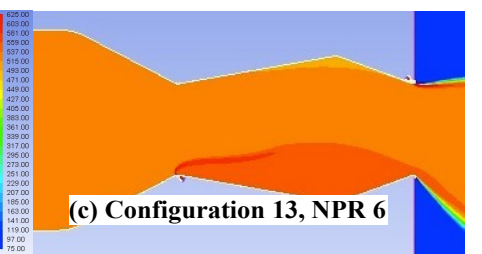
(c) Configuration 13, NPR 6



(a) Configuration 11, NPR 8



(b) Configuration 12, NPR 8



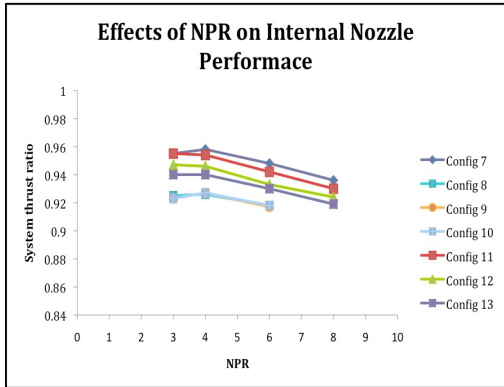
(c) Configuration 13, NPR 8

Figure 55: Total Temperature contours, configuration 11, 2.8% injection

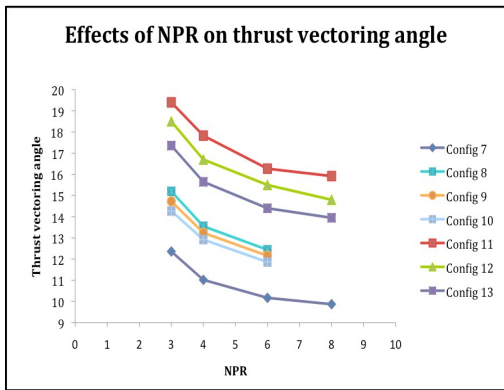
Figure 56: Total Temperature contours, configuration 12, 2.8% injection

**Figure 57: Total Temperature
contours, configuration 13, 2.8%
injection**

4. Comparison of the external and exit line injection



(a) System thrust ratio



(d) Discharge ratio

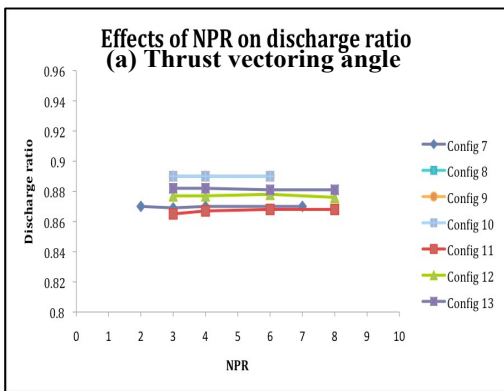


Figure 58: Comparison of configurations 7 through 13. 2.8% injection

The two cases studied in this paper are the tertiary injection at the tip and exit line at different angles. Figure 58 represents the system thrust ratio, thrust vectoring angle, and discharge ratio predictions for configurations 7 – 13. Figure 58a predicts that as the injection angle increase, the system thrust ratio increases for configuration 8 -13. However, the discharge coefficients from configurations 11 – 13 undesirability acts in reverse when compared to the system thrust ratio. The system thrust ratios of the configuration 8 – 10 were not expected to decrease since the tertiary injection was placed outside the nozzle, but the third term in equation 5 does lower the system thrust ratio. An average of 3.4% decrease was predicted due to this third term. Figure 58b can show that configuration 8 -13 provide much superior thrust vectoring angles as the injection angles increases. Configuration 11, with the most thrust vectoring angle, can provided up to 7.6% increase to configuration 7. Overall, it can be visualized that all current configurations studied in this paper can provide much higher thrust vectoring angles at an injection of 2.8% as compared to configuration 7. But, these high angels do decrease internal

nozzle performance.

The 3 best configurations from exit line and external tertiary injections are configuration 8, 11, and 12. Even though configuration 8 provides high discharge ratio, the thrust vectoring efficiency decreases by 3.7%. Thus, configurations 11 and 12 present the most efficient cases for this study. If compared to the non-injected flow from configuration 6, the system thrust ratio and the discharge ratio can decrease up to 2.5% and 8%. This decrease for the nozzle performances are not desirable, but they are trade offs that can be made to replace the mechanical thrust vectoring with the much lighter fluidic thrust vectoring.

Conclusion

A computational investigation has been completed to conform the effects of a tertiary injection for a dual throat nozzle. The configurations consisted of external and exit line tertiary injections at different angles. The results indicated that both the exit and external injections can dramatically increase the thrust vectoring angles. However, the decrease in system thrust ratio from the external injection lead to the favorability of exit line injections. After reviewing the internal performance and thrust vectoring angles, 2 of the exit line injections (configuration 11 and 12) were selected for providing the most efficient results. The two configurations were selected due their high performance for thrust vectoring efficiency, system thrust ratio, and the discharge ratio.

Furthermore, ANSYS Fluent's capability of calculating the exhaust flows of a dual throat nozzle was predicted. The system discharge ratio, thrust vectoring angle, and discharge coefficient were calculated and compared to experimental and computational results from NASA Langley. This conforms that ANSYS Fluent can provide steady state results for two-dimensional configurations with area ratio of 1. Just as all CFD codes, Fluent does have inaccuracies when calculating separation along walls, but it can predict the trends of the system thrust ratio, thrust vectoring angle, and discharge coefficient. CFD can be used to guide the study of DTN nozzles with secondary and tertiary injection, but experimental results are always required to verify the best configurations provided from CFD studies.

References

¹Deere, K. A.; Berrier, B. L.; Flamm, J. D.; and Johnson, S. K.: *A Computational Study of a Dual Throat Fluidic Thrust Vectoring Nozzle Concept*. AIAA-2003-3502, June 2005.

²Deere, K. A.; Berrier, B. L.; Flamm, J. D.; and Johnson, S. K.: *Computational Study of Fluidic Thrust Vectoring Using Separation Control in a Nozzle*. AIAA-2003-3803, June 2003.

³Flamm, J. D.; Deere, K. A.; Mason, M. L.; Berrier, B. L.; and Johnson, S. K.: *Experimental Study of an Axisymmetric Dual Throat Fluidic Thrust Vectoring Nozzle for a Supersonic Aircraft Application*. AIAA-2007-5084, July 2007.

⁴Banazadeh, A.; Saghafi, F.; Ghoreyshi, M.; and Pilidis, P.: *Experimental and computational investigation into the use of co-flow fluidic thrust vectoring on a small gas turbine*. The Aeronautical Journal, Vol. 17, No. 3117 January 2008.

⁵Hunter, C.A. and Deere, Karen A.: *Computational Investigation of Fluidic Counterflow Thrust Vectoring*. AIAA 99-2669, June 1999.

⁶Blake, B. A. : *Numerical Investigation of Fluidic Injection as a means of thrust control*. M.S. Thesis, University of New South Wales at the Australian Defense Force Academy. 2009.

⁷Waithe, K. A: *An Experimental and Computational Investigation of Multiple Injection Ports in a Convergent-Divergent Nozzle for Fluidic Thrust Vectoring*. GWU Master's Thesis, May 2001.

⁸Deere, K. A.: *Summary of Fluidic Thrust Vectoring Research Conducted at NASA Langley Research Center*. AIAA-2003-3800, June 2003.

⁹Deere, K. A.; Flamm, J. D.; Berrier, B. L.; and Johnson, S. K.: *Computational Study of an Axisymmetric Dual Throat Fluidic Thrust Vectoring Nozzle Concept for Supersonic Aircraft Application*. AIAA-2007-5085, July 2007.

¹⁰*A User's Guide to the Langley 16-Foot Transonic Tunnel Complex*, Revision 1. NASA TM-102750, 1990. (Supersedes NASA TM-83186)

¹¹Flamm, J. D.; Deere, K. A.; Mason, M. L.; Berrier, B. L.; and Johnson, S. K.: *Design Enhancements of the Two-Dimensional, Dual Throat Fluidic Thrust Vectoring Nozzle Concept*. AIAA-2006-3701, July 2006.

¹²FLUENT®, 2010, Version 13.0 ANSYS, Inc. Canonsburg, PA United States.

¹³Calson, J. R.: *High Reynolds Number Analysis of Flat plate and Separated Afterbody Flow Using Non-Linear Turbulence Models*. AIAA 96-2544, July 1996

¹⁴Asbury, S. A.: *Internal Performance of a Fixed-Shroud Nonaxisymmetric Nozzle Equipped with an Aft-Hood Exhaust Deflector*. NASA TM 97-206255, 1997.

¹⁵Anderson, J. D.: *Modern Compressible Flow: With Historical Perspective*, Third ed., McGraw-Hill, NY, 2003

¹⁶GridPro, 2000, Version 5.1, Program Development Company, White Plains, NY United States

¹⁷Mason, S. M.; and Crowther, J. W.: *Fluidic Thrust Vectoring of Low Observable Aircraft*. CEAS Aerospace Aerodynamics Research Conference. University of Manchester, School of Engineering, Cambridge, UK, June 2002

¹⁸Abdol-Hamid, K.S.: Application of a Multiblock/Multizone code(PAB3D) for the Three-Dimensional Navier-Stokes Equations. AIAA-91-2155, June 1999.